CHALMERS

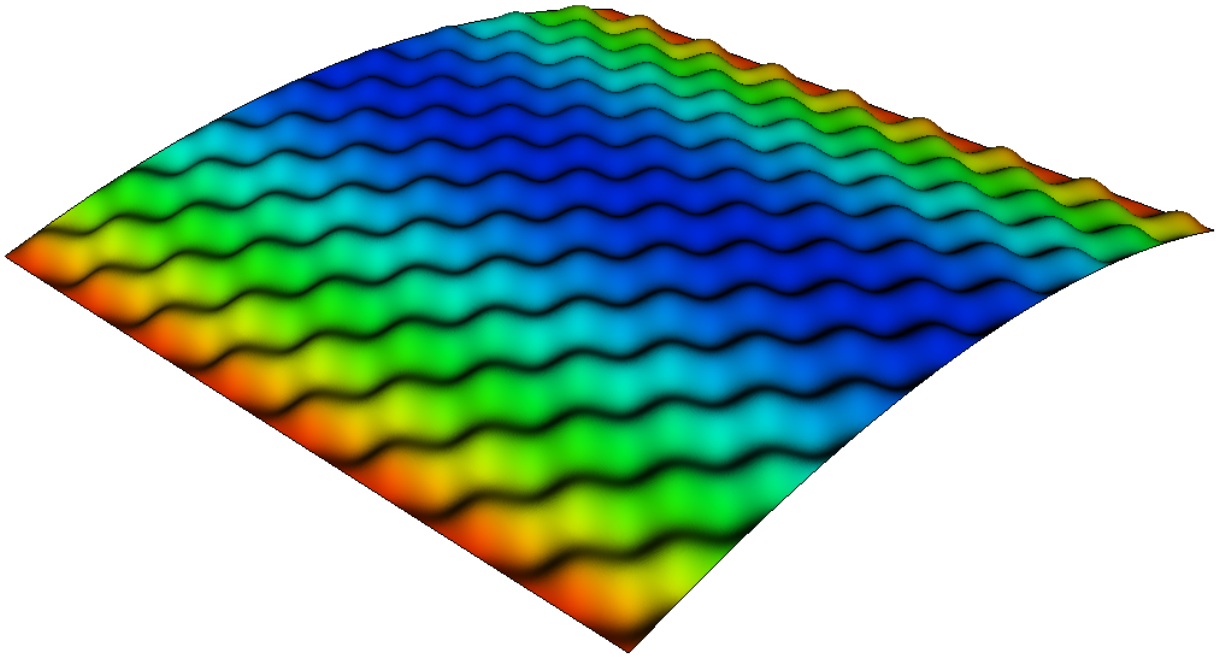

Homogenisation of embossed aluminium sheets using virtual material testing

Master's thesis in Applied Mechanics

SOFIA ALEXANDERSSON
FILIP LJUNGSTRÖM

Department of Industrial and Materials Science
CHALMERS UNIVERSITY OF TECHNOLOGY
Gothenburg, Sweden 2018

MASTER'S THESIS IN APPLIED MECHANICS

Homogenisation of embossed aluminium sheets using virtual material testing

SOFIA ALEXANDERSSON
FILIP LJUNGSTRÖM

Department of Industrial and Materials Science
Division of Material and Computational Mechanics
CHALMERS UNIVERSITY OF TECHNOLOGY

Gothenburg, Sweden 2018

Homogenisation of embossed aluminium sheets using virtual material testing
SOFIA ALEXANDERSSON
FILIP LJUNGSTRÖM

Department of Industrial and Materials Science
Division of Material and Computational Mechanics
Chalmers University of Technology
SE-412 96 Gothenburg
Sweden
Telephone: +46 (0)31-772 1000

Cover:
Deformation mode in bending for the embossed aluminium sheet in a finite element analysis.

Chalmers Reproservice
Gothenburg, Sweden 2018

Homogenisation of embossed aluminium sheets using virtual material testing
Master's thesis in Applied Mechanics
SOFIA ALEXANDERSSON
FILIP LJUNGSTRÖM
Department of Industrial and Materials Science
Division of Material and Computational Mechanics
Chalmers University of Technology

Abstract

As the demand for lightweight constructions increases, thin structured sheet metals become more and more popular in industrial applications. As a part of Volvo Cars' strive to lighten their vehicles, embossing is used to add stiffness to aluminium heat shields while keeping the mass unchanged. When analysing an embossed structural component using the finite element method, a very fine mesh is required to capture the geometry, meaning that a simulation of a fully resolved heat shield is computationally expensive. To enable analysis of the embossed structure, a virtual material model is developed in this thesis using homogenisation. This model describes the averaged macroscopic behaviour and enables the embossed sheet to be modelled as a flat structure.

The applied homogenisation method used to characterise the effective tensile and bending behaviours was virtual material testing. A representative volume element was established to model the embossed structure in finite element analyses with both Dirichlet and periodic boundary conditions. The virtual material model was verified using physical test data and simulation outputs from fully resolved structures.

The results showed that embossed sheets are stiffer in bending and weaker in tension, compared to flat structures with the same sheet thickness. Geometrical factors that influenced the behaviour were sheet thickness, pattern orientation, wavelength and amplitude. Comparisons between the virtual material model on flat sheets and fully resolved embossed models revealed that the homogenisation procedure predicts good tensile representation but a slightly too flexible bending behaviour.

However, when validating the model with physical test data, the results showed a too stiff response from the virtual material model. Since the model indicated good resemblance with the fully resolved finite element model, it was concluded that these inaccuracies probably were due to the neglect of some sheet characteristics in the modelling of the structure.

It was realised that the real thicknesses of the embossed sheets were lower than the nominal thicknesses specified by the manufacturers. By adjusting these values, the virtual material model showed better resemblance in bending, although it still predicted slightly too high natural frequencies. Possible error sources could for instance be residual stresses in the structure from the manufacturing process and a varying thickness throughout the pattern.

Keywords: Homogenisation, virtual material testing, embossed sheet, finite element method, representative volume element, orthotrophy, periodic boundary conditions, structured sheet

Preface

This thesis was performed as the concluding part of our studies in the Applied Mechanics master's programme at Chalmers University of Technology. The research was carried out at FS Dynamics in Gothenburg on behalf of Volvo Cars. Examiner at Chalmers University of Technology was Dr. Magnus Ekh and supervisor at FS Dynamics was Lic. Johanna Lilja.

Acknowledgements

Firstly, we would like to thank our examiner Magnus Ekh for invaluable input and feedback during the project. We would especially like to thank Johanna Lilja for the time she put aside to patiently supervise us throughout the project, and for the pieces of advice we have received which have helped us improve our work. Also, a big thanks to Robert Lillbacka at FS Dynamics who helped us better understand homogenisation and supported us when structuring the project.

Many thanks to Niklas Flöe at Volvo Cars for assisting us with information and test data related to the heat shield, and to Fredrik Larsson at Chalmers University of Technology for valuable discussions about homogenisation. Furthermore, we are very grateful to Björn Andersson for his enthusiasm for our project and for sharing his simulation expertise with us. Lastly, we want to express our gratitude to Caroline Olofsson, Emma Sundell and all employees at FS Dynamics for always making us feel like home at the office.

Sofia Alexandersson and Filip Ljungström,
Gothenburg, 2018

Nomenclature

Acronyms

DBC	Dirichlet Boundary Condition
FE	Finite Element
FEA	Finite Element Analysis
MPC	Multi Point Constraints
PBC	Periodic Boundary Condition
RVE	Representative Volume Element
VE	Volume Element

Symbols

Γ	Boundary
$\underline{\hat{n}}$	Normal vector
ν	Poisson's ratio
Ω	Domain
ρ	Density
ρ_A	Surface density
$\underline{\tilde{\alpha}}$	Rotation fluctuations
$\underline{\alpha}$	Rotations
$\underline{\epsilon^0}$	Mid-plane strains
$\underline{\epsilon}$	Strains
$\underline{\kappa}$	Curvatures
$\underline{\sigma}$	Stresses
$\underline{A}$	Extensional stiffness matrix
$\underline{B}$	Coupling stiffness matrix
$\underline{b}$	Distributed load xy-plane
$\underline{C}$	Stiffness matrix
$\underline{D}$	Bending stiffness matrix
$\underline{F}$	Force vector
$\underline{H}$	Deformation gradient
$\underline{H}^{\kappa}$	Rotation gradient
$\underline{M}$	Reaction moments
$\underline{N}$	Reaction forces
$\underline{Q}$	Orthotropic stiffness matrix
$\underline{u}$	Displacements

$\underline{w}$	Displacement fluctuations
$\underline{x}$	Position vector
A	Area
E	Elastic modulus
G	Shear modulus
k	Relative stiffness
L	Plate length
q	Distributed load z-direction
t	Thickness
w	Out-of-plane displacement

Contents

1 Introduction

A current development trend in the automotive industry is to improve the vehicles environmental performance. Since the vehicle weight is one of the main factors that affect fuel economy and exhaust emissions, weight reduction is a common pursuit amongst manufacturers [1]. As a result, industries are adopting advanced materials and evaluating new innovative designs. A technique used at Volvo Cars is to lighten the vehicles by reducing the thicknesses of metal sheets used at various places of the car.

This is done to an aluminium heat shield positioned under the car that protects the rear parts from the exhaust system, see Figure 1.1. To save weight, it is desirable to have the heat shield as thin as possible, but since structural stiffness decreases with reduced thickness, this could lead to problems with large deformations and fatigue. Instead, sheets with the embossed pattern illustrated in Figure 1.2 are used to add stiffness to the heat shield while keeping the mass unchanged [2].

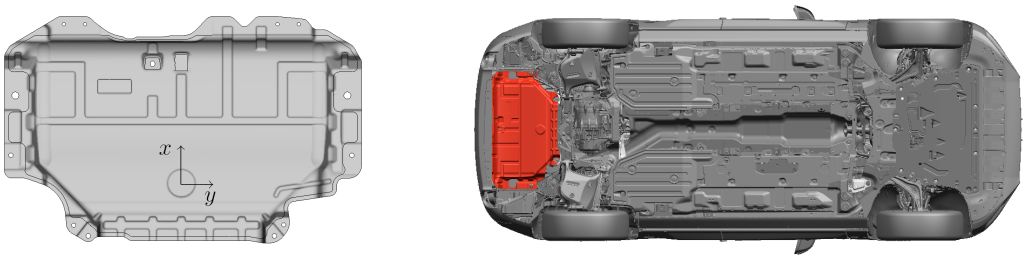

Figure 1.1: Heat shield geometry and placement.

The change of structural design implies new testing to verify the shield's performance. Since physical testing is expensive and time-consuming, it is desirable to perform simulations using Finite Element Analysis (FEA). Due to the small length-scales of the embossed pattern, wavelengths of less than 2 mm compared to a shield area of 0.5 m^2, the geometry can not be fully resolved without a very fine mesh. This implies computationally expensive simulations. Instead, it is proposed to homogenise the structure to create a virtual material model that takes the embossed behaviour into account and enables FEA on a flat shield model with equivalent structural properties, which allows for a coarser mesh.

During the spring of 2018, a thesis was written by Cai Öhrvall on behalf of Volvo Cars with the aim of conducting physical tests of the embossed aluminium shields [3]. Data presented was for instance the structure's natural frequencies and flexibility. The test results will be used as reference to validate the virtual material model.

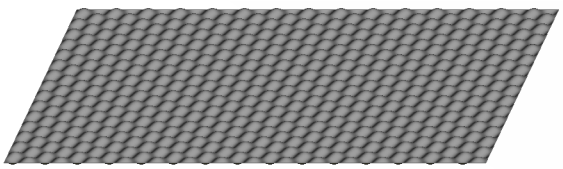

Figure 1.2: Embossed sheet pattern.

1.1 Purpose

The purpose of this master thesis is to use homogenisation to develop a virtual material that enables an embossed sheet structure to be modelled as a flat sheet. This would reduce the computational power needed to capture the embossed behaviour, since the embossed pattern would not need to be resolved.

1.2 Method

Initially, a finite element model of the embossed sheet structure will be developed and a meso-scale model of the structure, a Representative Volume Element (RVE), will be introduced. This model will be used for homogenisation according to the method virtual material testing. Together with the RVE, boundary conditions and material properties will be used in the virtual tests which will yield a macroscopic response of the structure. This response will be used to establish the virtual material model. The schematics of the homogenisation method is illustrated in Figure 1.3.

The virtual material model will be applied on flat sheets and verified using physical test data and results from embossed model simulations. Additional investigations will be carried out to study relations between the material response and geometrical parameters such as sheet thickness and pattern amplitude.

The simulations will be performed using ANSA [4] as pre-processor, Abaqus/Standard 2016 [5] as FEA implicit solver and META [6] as post-processor along with Matlab [7] for data-processing.

1.3 Limitations

This thesis will have the following limitations:

- Elastic behaviour will be assumed for the sheet and thus no plastic behaviour will be accounted for.
- Although rolled sheet metal may have residual stresses from its manufacturing process, it is neglected in the analyses.
- Even if the sheet thickness may vary along the embossed pattern, it will be considered as constant.
- All simulations assumes room temperature.

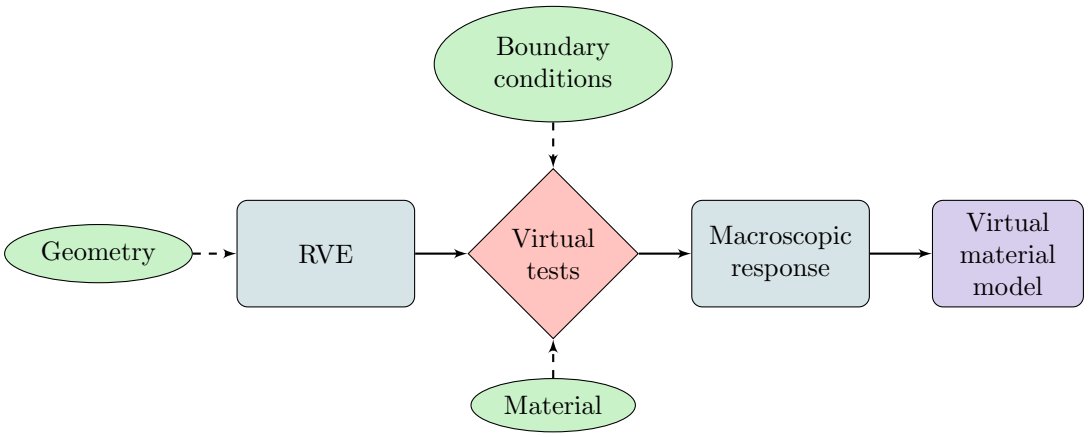

Figure 1.3: Schematics of the homogenisation method virtual material testing.

2 Theoretical Framework

This chapter describes the theory behind the structural analysis together with the homogenisation technique and boundary conditions. Key concepts and assumptions in the modelling of the embossed shield are presented as well.

2.1 Kirchhoff-Love plate theory

The Kirchhoff-Love theory is a mathematical model describing the behaviour of thin plates. By making assumptions on the behaviour of the mid-surface plane, the theory reduces a three-dimensional problem to a two-dimensional form.

The typical definition of a thin plate is a plane structure with length and width dimensions that are at least 10 times larger than the plate thickness [8]. This criterion is fulfilled by the homogenised macro-structure that will be represented by plate elements and the virtual material model. When evaluating the embossed pattern in the meso-structure, shell elements in Abaqus will be used. More information about how these are implemented can be found in [9].

2.1.1 Equilibrium

Consider a small element of a thin plate exposed to a distributed load q in z-direction and a distributed load $\underline{b}$ in the xy-plane, as shown in Figure 2.1. The internal forces and moments per unit length acting on this plate are the cross-sectional membrane forces $\underline{N}$, the shear forces $\underline{V}$ and the bending moments $\underline{M}$.

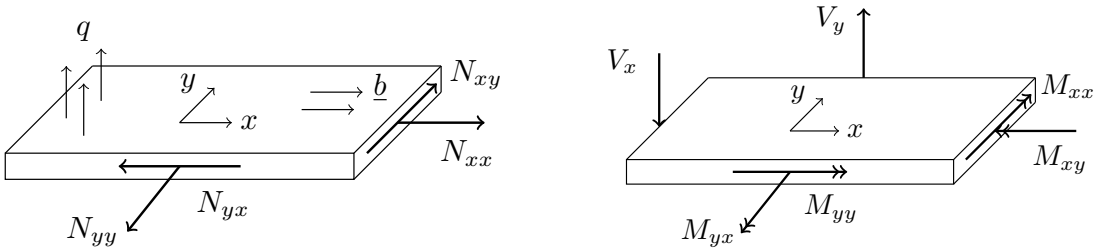

Figure 2.1: Definition of cross-sectional quantities in a rectangular plate.

By evaluating force and moment equilibrium, the governing plate equations, together with the gradient operators $\tilde{\nabla}$ and ∇, are defined as [10]:

$$\begin{cases} -\tilde{\nabla}^T \underline{N} = \underline{b} \\ -\nabla^T \underline{V} = q \\ \tilde{\nabla}^{\mathrm{T}} \underline{M} - \underline{V} = \underline{0} \end{cases} \tag{2.1}$$

$$\tilde{\nabla} = \begin{bmatrix} \frac{\partial}{\partial x} & 0 \\ 0 & \frac{\partial}{\partial y} \\ \frac{\partial}{\partial x} & \frac{\partial}{\partial y} \end{bmatrix}, \qquad \nabla = \begin{bmatrix} \frac{\partial}{\partial x} \\ \frac{\partial}{\partial y} \end{bmatrix} \tag{2.2}$$

Here, the resultant forces and moments acting on a cross-section are defined in terms of the stress components $\underline{\sigma}$ and $\underline{\tau}$, and the thickness t as follows (see details in [10]):

$$\underline{N} = \begin{bmatrix} N_{xx} \\ N_{yy} \\ N_{xy} \end{bmatrix} = \int_{-t/2}^{t/2} \begin{bmatrix} \sigma_{xx} \\ \sigma_{yy} \\ \sigma_{xy} \end{bmatrix} \mathrm{d}z = \int_{-t/2}^{t/2} \underline{\sigma}\, \mathrm{d}z \tag{2.3}$$

$$\underline{V} = \begin{bmatrix} V_x \\ V_y \end{bmatrix} = \int_{-t/2}^{t/2} \begin{bmatrix} \sigma_{xz} \\ \sigma_{yz} \end{bmatrix} \mathrm{d}z = \int_{-t/2}^{t/2} \underline{\tau}\, \mathrm{d}z \tag{2.4}$$

$$\underline{M} = \begin{bmatrix} M_{xx} \\ M_{yy} \\ M_{xy} \end{bmatrix} = \int_{-t/2}^{t/2} z \begin{bmatrix} \sigma_{xx} \\ \sigma_{yy} \\ \sigma_{xy} \end{bmatrix} \mathrm{d}z = \int_{-t/2}^{t/2} z\, \underline{\sigma}\, \mathrm{d}z \tag{2.5}$$

2.1.2 Kinematics

The Kirchhoff-Love theory assumes that planes in the normal direction to the plate's mid-surface remains straight as well as normal to the mid-surface during deformation. It also assumes that the plate thickness remains the same [11]. These kinematic assumptions result in displacements according to [10]:

$$\underline{u} = \begin{bmatrix} u_x \\ u_y \end{bmatrix} = \underline{u}^0 - z\nabla w \tag{2.6}$$

In the equation, $\underline{u}^0(x, y) = [u_x^0\ u_y^0]^T$ are the in-plane displacements at the mid-plane ($z = 0$) and w is the transverse deflection. The displacement in z-direction is assumed to be constant throughout the thickness of the plate and is equal to w. This results in the following strains [10]:

$$\underline{\epsilon} = \begin{bmatrix} \epsilon_{xx} \\ \epsilon_{yy} \\ 2\epsilon_{xy} \end{bmatrix} = \tilde{\nabla}\underline{u} = \tilde{\nabla}\underline{u}^0 - z\overset{*}{\nabla}w = \underline{\epsilon}^0 - z\underline{\kappa}\,, \qquad \overset{*}{\nabla} = \tilde{\nabla}\nabla = \begin{bmatrix} \frac{\partial^2}{\partial x^2} \\ \frac{\partial^2}{\partial y^2} \\ 2\frac{\partial^2}{\partial x \partial y} \end{bmatrix} \tag{2.7}$$

$$\underline{\gamma} = \begin{bmatrix} \epsilon_{xz} \\ \epsilon_{yz} \end{bmatrix} = \underline{0} \tag{2.8}$$

Here, $\underline{\epsilon}^0$ and $\underline{\kappa}$ are the mid-plane strains and plate curvatures, respectively.

2.1.3 Approximation of strains and curvatures

For the boundary conditions of the homogenised plate element presented in Section 2.3, the mid-plane strains and plate curvatures will be used with the following approximation.

The mid-plane strains $\underline{\epsilon}^0$ are defined as the ratio of mid-plane displacement u^0 to the original plate lengths L_x and L_y presented in Figure 2.2. The definitions are approximated as:

$$\underline{\epsilon}^0 = \tilde{\nabla}\underline{u}^0 = \begin{bmatrix} \epsilon^0_{xx} \\ \epsilon^0_{yy} \\ 2\epsilon^0_{xy} \end{bmatrix} = \begin{bmatrix} \frac{\partial u^0_x}{\partial x} \\ \frac{\partial u^0_y}{\partial y} \\ \frac{\partial u^0_y}{\partial x} + \frac{\partial u^0_x}{\partial y} \end{bmatrix} \approx \begin{bmatrix} \frac{-u^0_x(\frac{-L_x}{2}) + u^0_x(\frac{L_x}{2})}{L_x} \\ \frac{-u^0_y(\frac{-L_y}{2}) + u^0_y(\frac{L_y}{2})}{L_y} \\ \frac{-u^0_y(\frac{-L_x}{2}) + u^0_y(\frac{L_x}{2})}{L_x} + \frac{-u^0_x(\frac{-L_y}{2}) + u^0_x(\frac{L_y}{2})}{L_y} \end{bmatrix} \tag{2.9}$$

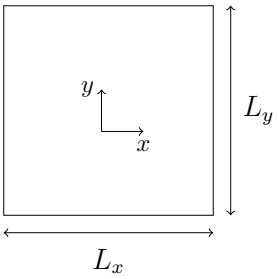

Figure 2.2: Illustration of the plate lengths L_x and L_y.

The plate curvatures $\underline{\kappa}$ are defined as the change of the slope angle α with respect to arc length s, i.e. for the x-direction $\kappa_{xx} = d\alpha_y/ds$. Figure 2.3 illustrates the geometry of a plate, where the red line denotes a deformed plate with an arc length s. For small angles, $\alpha_y \approx \tan(\alpha_y) = \partial w/\partial x$ and $\mathrm{d}\alpha_y/\mathrm{d}s \approx \partial\alpha_y/\partial x$, and similarly in the y-direction [12]. This means that the curvatures can be approximated as:

$$\underline{\kappa} = \overset{*}{\nabla} w = \begin{bmatrix} \kappa_{xx} \\ \kappa_{yy} \\ 2\kappa_{xy} \end{bmatrix} = \begin{bmatrix} \frac{\partial^2 w}{\partial x^2} \\ \frac{\partial^2 w}{\partial y^2} \\ 2\frac{\partial^2 w}{\partial x \partial y} \end{bmatrix} \approx \begin{bmatrix} \frac{\partial \alpha_y}{\partial x} \\ \frac{\partial \alpha_x}{\partial y} \\ 2\frac{\partial \alpha_x}{\partial x} \approx 2\frac{\partial \alpha_y}{\partial y} \end{bmatrix} \approx \begin{bmatrix} \frac{-\alpha_y(\frac{-L_x}{2}) + \alpha_y(\frac{L_x}{2})}{L_x} \\ \frac{-\alpha_x(\frac{-L_y}{2}) + \alpha_x(\frac{L_y}{2})}{L_y} \\ \frac{2\left(-\alpha_x(\frac{-L_x}{2}) + \alpha_x(\frac{L_x}{2})\right)}{L_x} \approx \frac{2\left(-\alpha_y(\frac{-L_y}{2}) + \alpha_y(\frac{L_y}{2})\right)}{L_y} \end{bmatrix} \tag{2.10}$$

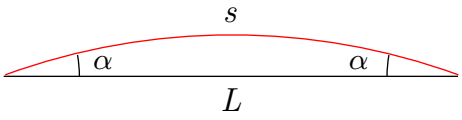

Figure 2.3: Illustration assisting the curvature approximation.

2.1.4 Constitutive model

The mechanical properties of a material are defined from constitutive models that describe how the material responds to various loading. For a linear elastic material, Hooke's generalized law describes the relation between stresses, σ_{ij}, and strains, ϵ_{kl}, in a structure:

$$\sigma_{ij} = C_{ijkl}\epsilon_{kl} \tag{2.11}$$

Here, C_{ijkl} is the 4th order stiffness tensor with 81 components. The most general case of anisotropy uses a stiffness tensor with only 21 independent components [11]. Anisotropy refers to a material with properties that vary in different directions. If a material instead is orthotropic, it has three orthogonal planes of symmetry and

properties that differ in three directions, usually x, y and z in a cartesian coordinate system. In this case, the stiffness tensor $\underline{C}$ is reduced to 9 independent components according to [13]:

$$\begin{bmatrix} \sigma_{xx} \\ \sigma_{yy} \\ \sigma_{zz} \\ \sigma_{yz} \\ \sigma_{xz} \\ \sigma_{xy} \end{bmatrix} = \begin{bmatrix} C_{11} & C_{12} & C_{13} & 0 & 0 & 0 \\ & C_{22} & C_{23} & 0 & 0 & 0 \\ & & C_{33} & 0 & 0 & 0 \\ & & & C_{44} & 0 & 0 \\ & \text{sym} & & & C_{55} & 0 \\ & & & & & C_{66} \end{bmatrix} \begin{bmatrix} \epsilon_{xx} \\ \epsilon_{yy} \\ \epsilon_{zz} \\ \epsilon_{yz} \\ \epsilon_{xz} \\ \epsilon_{xy} \end{bmatrix} \tag{2.12}$$

For thin plates it can be assumed that the out-of-plane stresses are zero, i.e. $\sigma_{zz} = \sigma_{xz} = \sigma_{yz} = 0$ [11]. This means that the relation can be simplified even further according to both orthotropy and plane stress conditions [14]. This is described by introducing the reduced stiffness matrix $\underline{Q}$:

$$\begin{bmatrix} \sigma_{xx} \\ \sigma_{yy} \\ \sigma_{xy} \end{bmatrix} = \begin{bmatrix} Q_{11} & Q_{12} & 0 \\ Q_{12} & Q_{22} & 0 \\ 0 & 0 & Q_{66} \end{bmatrix} \begin{bmatrix} \epsilon_{xx} \\ \epsilon_{yy} \\ 2\epsilon_{xy} \end{bmatrix} \tag{2.13}$$

where $\underline{Q}$ is defined as:

$$\underline{Q} = \frac{1}{1 - \nu_{xy}\nu_{yx}} \begin{bmatrix} E_x & \nu_{xy}E_y & 0 \\ \nu_{yx}E_x & E_y & 0 \\ 0 & 0 & G_{xy}(1 - \nu_{xy}\nu_{yx}) \end{bmatrix} \tag{2.14}$$

Here, E is the elastic modulus in the different directions, ν the Poisson's ratio and G the shear modulus. The Poisson's ratio ν_{yx} is defined as $\nu_{yx} = (E_y/E_x)\nu_{xy}$ [14].

2.1.5 Stiffness matrices

Based on the definition of $\underline{\epsilon}$ in Equation 2.7, the plate's mid-plane strains $\underline{\epsilon}^0$ and curvatures $\underline{\kappa}$ can be related to the reaction forces $\underline{N}$ and moments $\underline{M}$ according to:

$$\begin{bmatrix} \underline{N} \\ \underline{M} \end{bmatrix} = \begin{bmatrix} \underline{A} & \underline{B} \\ \underline{B} & \underline{D} \end{bmatrix} \begin{bmatrix} \underline{\epsilon}^0 \\ \underline{\kappa} \end{bmatrix} \tag{2.15}$$

In these relations, $\underline{A}$ is the extensional stiffness matrix, $\underline{B}$ the coupling stiffness matrix and $\underline{D}$ the bending stiffness matrix. $\underline{A}$ represents the behaviour in tension/compression, $\underline{D}$ represents the behaviour in bending and $\underline{B}$ represents the coupling between the two [14]. Fully expanded, Equation 2.15 writes:

$$\begin{bmatrix} N_{xx} \\ N_{yy} \\ N_{xy} \\ \\ M_{xx} \\ M_{yy} \\ M_{xy} \end{bmatrix} = \begin{bmatrix} A_{11} & A_{12} & A_{16} & B_{11} & B_{12} & B_{16} \\ A_{12} & A_{22} & A_{26} & B_{12} & B_{22} & B_{26} \\ A_{16} & A_{26} & A_{66} & B_{16} & B_{26} & B_{66} \\ & & & & & \\ B_{11} & B_{12} & B_{16} & D_{11} & D_{12} & D_{16} \\ B_{12} & B_{22} & B_{26} & D_{12} & D_{22} & D_{26} \\ B_{16} & B_{26} & B_{66} & D_{16} & D_{26} & D_{66} \end{bmatrix} \begin{bmatrix} \epsilon^0_{xx} \\ \epsilon^0_{yy} \\ 2\epsilon^0_{xy} \\ \\ \kappa_{xx} \\ \kappa_{yy} \\ 2\kappa_{xy} \end{bmatrix} \tag{2.16}$$

By combining Equations 2.3, 2.5, 2.13 and 2.15, the stiffness matrices are obtained as:

$$\underline{A} = \frac{t}{1-\nu_{xy}\nu_{yx}} \begin{bmatrix} E_x & \nu_{xy}E_y & 0 \\ \nu_{yx}E_x & E_y & 0 \\ 0 & 0 & G_{xy}(1-\nu_{xy}\nu_{yx}) \end{bmatrix} \tag{2.17}$$

$$\underline{B} = \frac{t^2}{4(1-\nu_{xy}\nu_{yx})} \begin{bmatrix} E_x & \nu_{xy}E_y & 0 \\ \nu_{yx}E_x & E_y & 0 \\ 0 & 0 & G_{xy}(1-\nu_{xy}\nu_{yx}) \end{bmatrix} \tag{2.18}$$

$$\underline{D} = \frac{t^3}{12(1-\nu_{xy}\nu_{yx})} \begin{bmatrix} E_x & \nu_{xy}E_y & 0 \\ \nu_{yx}E_x & E_y & 0 \\ 0 & 0 & G_{xy}(1-\nu_{xy}\nu_{yx}) \end{bmatrix} \tag{2.19}$$

2.1.6 Coordinate transformation

By using the transformation matrices $\underline{T}_1$ and $\underline{T}_2$, from Equations 2.20 and 2.21 [14], the orthotropic material properties in plane stress can be transformed to a coordinate system that is rotated an angle θ around the out-of-plane z-axis [14].

$$\underline{T}_1 = \begin{bmatrix} \cos^2\theta & \sin^2\theta & 2\sin\theta\cos\theta \\ \sin^2\theta & \cos^2\theta & -2\sin\theta\cos\theta \\ -\sin\theta\cos\theta & \sin\theta\cos\theta & \cos^2\theta - \sin^2\theta \end{bmatrix} \tag{2.20}$$

$$\underline{T}_2 = \begin{bmatrix} \cos^2\theta & \sin^2\theta & \sin\theta\cos\theta \\ \sin^2\theta & \cos^2\theta & -\sin\theta\cos\theta \\ -2\sin\theta\cos\theta & 2\sin\theta\cos\theta & \cos^2\theta - \sin^2\theta \end{bmatrix} \tag{2.21}$$

The stiffness matrices, i.e. $\underline{A}$, could then be written as the transformed matrix $\underline{A}_\theta$ by:

$$\underline{A}_\theta = \underline{T}_1^{-1}\, \underline{A}\, \underline{T}_2 \tag{2.22}$$

2.2 Homogenisation

Homogenisation is a method used to study the relationship between a local non-homogeneous structure and its macroscopic behaviour. Two scales of a structure are introduced; a macro-scale that represents a continuum with homogenised properties, and a meso-scale that refers to a smaller scale where the structure's heterogeneity is taken into account. Homogenisation enables a prediction of the structure's behaviour on a macro-scale by taking local heterogeneity into account [2]. Often, the homogenisation can be used to define a macroscopic model. Hence, the macroscopic model can predict the average properties of the meso-scale structure [15]. Figure 2.4 illustrates the method where C_1 and C_2 represent heterogeneous properties on the meso-scale that influence the response $\bar{C}$ on the macro-scale.

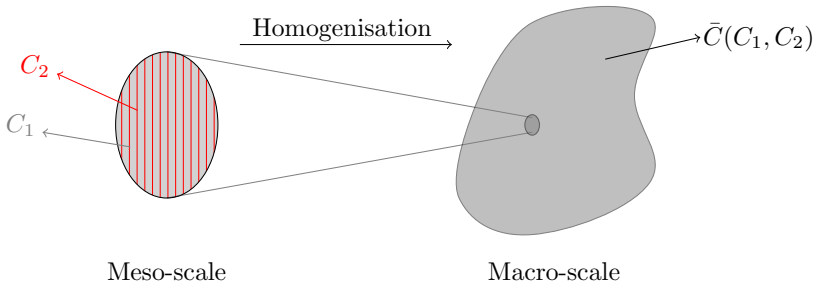

Figure 2.4: General homogenisation concept.

Figure 2.5 shows the homogenisation method that will be used for embossed sheets. Here the local heterogeneity is the geometry's pattern, C_{geom}. On the macro-scale, the material properties of the embossed sheet $\bar{C}$ are functions of both C_{geom} and the reference material C_{mat}. Since the homogenised material $\bar{C}$ is not a real material, this is often referred to as a *virtual material*. This virtual material will be dependent on the geometry, so it could also be called a *virtual structure*, but in this thesis the notation virtual material will be used.

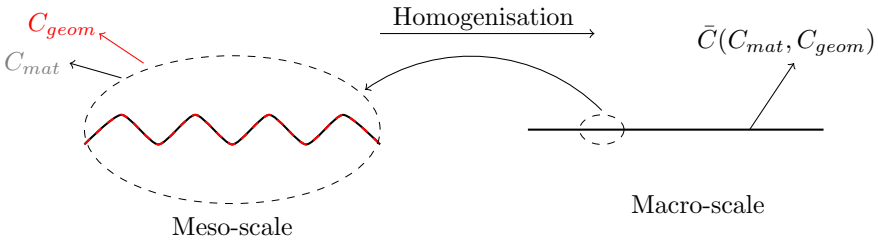

Figure 2.5: Homogenisation concept for the embossed structure.

2.2.1 Representative volume element

To find the behaviour of the meso-scale structure, simulations are carried out on a representative volume element (RVE). The RVE is the smallest volume element that will yield values that can represent the macro-scale model. The size of the RVE should fulfil the following conditions based on its length scale L_{RVE} [15]:

- The RVE should be small compared to the macro-scale, $L_{RVE} << L_{macro}$
- The RVE should be large enough to capture the meso-scale's heterogeneous behaviour

2.2.2 Virtual material testing

In order to find the macroscopic properties of the embossed sheet, the $\underline{A}$, $\underline{B}$ and $\underline{D}$ matrices from Equation 2.15 are identified using a method called *virtual material testing*. The approach is to subject the RVE to boundary conditions in form of mid-plane strains $\underline{\epsilon}^0$ and curvatures $\underline{\kappa}$, and then extract the reaction forces $\underline{N}$ and reaction moments $\underline{M}$ from the deformed structure. A schematic of this method is presented in Figure 2.6.

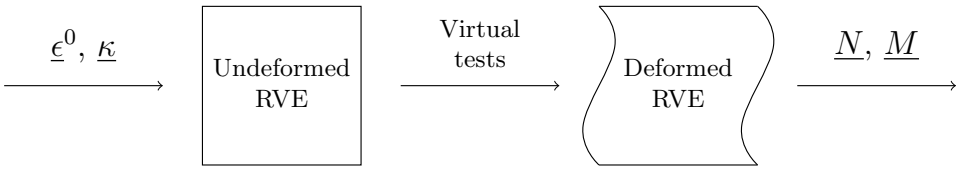

Figure 2.6: Flow chart describing the virtual material testing procedure.

By sequentially applying one component from $\underline{\epsilon} = [\epsilon^0_{xx}\ \epsilon^0_{yy}\ 2\epsilon^0_{xy}\ \kappa_{xx}\ \kappa_{yy}\ 2\kappa_{xy}]^T$ whilst keeping the others zero, the entire $\underline{A}$, $\underline{B}$ and $\underline{D}$ matrices from Equation 2.15 can be identified. These form the basis of the virtual material model that describes the macroscopic behaviour of the embossed metal sheet.

2.3 Boundary conditions

These section explains the theory behind the two types of boundary conditions that will be evaluated for the virtual testing procedure; Dirichlet Boundary Conditions (DBC) and Periodic Boundary Conditions (PBC). Both conditions can be used to apply average mid-plain strains $\bar{\epsilon}^0_i$ or curvatures $\bar{\kappa}_i$ to the RVE by prescribing displacements, u_i, or rotations, α_i.

The displacement gradient H_{ij} is defined as:

$$H_{ij} = \frac{\partial u_i}{\partial x_j} \tag{2.23}$$

where x_j is the position vector. The macroscopic displacement gradient $\bar{H}_{ij}$ is defined as the area weighted average of the meso-scale displacement gradient H_{ij}. With Gauss theorem, it can be rewritten as an boundary integral:

$$\bar{H}_{ij} = \frac{1}{A}\int_\Omega H_{ij}\,\mathrm{d}A = \frac{1}{A}\int_\Omega \frac{\partial u_i}{\partial x_j}\,\mathrm{d}A = \frac{1}{A}\int_\Gamma \hat{n}_j u_i\,\mathrm{d}\Gamma \tag{2.24}$$

It is assumed that the displacement is zero, $u_i = 0_i$, at origo. This gives the deformation Δu as:

$$\Delta u_i = u_i(x) - u_i(0) = u_i(x) \tag{2.25}$$

The rotation gradient $H^\kappa_{ij} = \partial\alpha_i/\partial x_j$, can in the same way as the deformation gradient in Equation 2.24 be written as the macroscopic rotation gradient $\bar{H}^\kappa_{ij}$, as:

$$\bar{H}^\kappa_{ij} = \frac{1}{A}\int_\Omega \frac{\partial \alpha_i}{\partial x_j}\,\mathrm{d}A = \frac{1}{A}\int_\Gamma \hat{n}_j \alpha_i\,\mathrm{d}\Gamma \tag{2.26}$$

2.3.1 Dirichlet boundary conditions

This section describes the theory behind the Dirichlet boundary conditions. Using Equation 2.25, the displacement is written as:

$$\Delta u_i = u_i \approx \bar{H}_{ij}\Delta x_j = \bar{H}_{ij}x_j \quad \text{on } \Gamma \tag{2.27}$$

Combining Equation 2.24 and 2.27 and using the backward Gauss theorem, the macroscopic deformation gradient becomes:

$$\bar{H}_{ij} = \frac{1}{A}\int_\Gamma \hat{n}_j \bar{H}_{ik}x_k\,\mathrm{d}\Gamma = \frac{\bar{H}_{ik}}{A}\int_\Gamma \hat{n}_j x_k\,\mathrm{d}\Gamma = \frac{\bar{H}_{ik}}{A}\underbrace{\int_\Omega \frac{\partial x_k}{\partial x_j}\,\mathrm{d}A}_{=\delta_{kj}A} = \frac{\bar{H}_{ik}\delta_{kj}A}{A} = \bar{H}_{ij} \tag{2.28}$$

which proves that the prescribed displacement in Equation 2.27 results in the correct average displacement gradient.

Similar to Equation 2.27 and 2.28 the rotation and rotation gradient becomes:

$$\alpha_i = \bar{H}^{\kappa}_{ij} x_j \quad \text{on } \Gamma \tag{2.29}$$

$$\bar{H}^{\kappa}_{ij} = \frac{1}{A}\int_{\Gamma} \hat{n}_j \bar{H}^{\kappa}_{ij} x_k \, \mathrm{d}\Gamma = \frac{\bar{H}^{\kappa}_{ij}}{A}\int_{\Gamma} \hat{n}_j x_k \, \mathrm{d}\Gamma = \bar{H}^{\kappa}_{ij} \tag{2.30}$$

2.3.2 Periodic boundary conditions

Periodic boundary conditions are used to achieve the impression of a domain that is larger than its actual size, which is desirable for an RVE representing the macro-scale of a structure. PBC are doing this by simulating that the domain is repeating itself at each boundary.

Theory

The PBC are structured in the same way as the DBC, but with the addition of a displacement fluctuation, w_i. The displacement is defined as:

$$u_i = \bar{H}_{ij} x_j + w_i \quad \text{on } \Gamma \tag{2.31}$$

This is illustrated in Figure 2.7, where the deformation of PBC and DBC are shown together with the undeformed RVE. The difference is that the boundaries prescribed with PBC are allowed to fluctuate from the mean displacement, but with the conditions that the fluctuation is equal on opposite sides of the RVE.

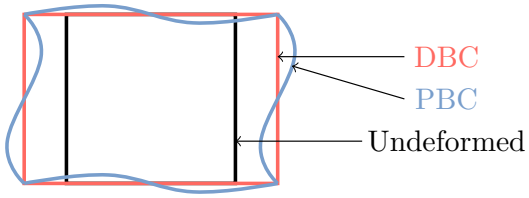

Figure 2.7: The fluctuations allowed by the PBC, a difference compared to DBC.

The macroscopic deformation gradient for PBC is defined as:

$$\bar{H}_{ij} = \frac{1}{A}\int_{\Omega} \frac{\partial u_i}{\partial x_j} \, \mathrm{d}A = \underbrace{\bar{H}_{ij}}_{Dirichlet} + \frac{1}{A}\underbrace{\int_{\Omega} \frac{\partial w_i}{\partial x_j} \, \mathrm{d}A}_{\int_{\Gamma} \hat{n}_j w_i \, \mathrm{d}\Gamma} \tag{2.32}$$

It is hence the same definition as for the DBC, but with a fluctuation term introduced. If the fluctuations are equal at opposite sides, $w^+ = w^-$ (referring to the notations in Figure 2.8), then the fluctuation term is expanded to:

$$\int_{\Gamma} \hat{n}_j w_i \, \mathrm{d}\Gamma = \int_{\Gamma^+} \hat{n}^+_j w^+_i \, \mathrm{d}\Gamma + \int_{\Gamma^-} \hat{n}^-_j w^-_i \, \mathrm{d}\Gamma \tag{2.33}$$

In a symmetric domain, such as Figure 2.8, $\Gamma^- = \Gamma^+$ and $\hat{n}^-_j = -\hat{n}^+_j$, Equation 2.33 cam be written:

$$\int_{\Gamma} \hat{n}^+_j \left(w^+_i - w^-_i\right) \mathrm{d}\Gamma = 0_{ij} \tag{2.34}$$

and hence, the correct average displacement gradient is obtained also for PBC.

Similarly, a rotation fluctuation $\tilde{\alpha}_i$ is introduced, such that the rotation at the boundaries is written:

$$\alpha_i = \bar{H}^{\kappa}_{ij} x_j + \tilde{\alpha}_i \quad \text{on } \Gamma \tag{2.35}$$

This gives the macroscopic rotation gradient for PBC as:

$$\bar{H}^{\kappa}_{ij} = \frac{1}{A}\int_{\Omega} \frac{\partial \alpha_i}{\partial x_j}\,\mathrm{d}A = \underbrace{\bar{H}^{\kappa}_{ij}}_{Dirichlet} + \frac{1}{A}\underbrace{\int_{\Omega} \frac{\partial \tilde{\alpha}_i}{\partial x_j}\,\mathrm{d}A}_{\int_{\Gamma} \hat{n}_j \tilde{\alpha}_i \,\mathrm{d}\Gamma} \tag{2.36}$$

If assuming that the rotation fluctuations are equal at opposite sides, $\tilde{\alpha}^{-}_i = \tilde{\alpha}^{+}_i$, the fluctuation term in Equation 2.36 is expanded to:

$$\int_{\Gamma} \hat{n}_j \tilde{\alpha}_i \mathrm{d}\Gamma = \int_{\Gamma^+} \hat{n}^{+}_j \tilde{\alpha}^{+}_i \,\mathrm{d}\Gamma + \int_{\Gamma^-} \hat{n}^{-}_j \tilde{\alpha}^{-}_i \,\mathrm{d}\Gamma \tag{2.37}$$

Assuming a symmetric domain, $\Gamma^- = \Gamma^+$ and $\hat{n}^{-}_j = -\hat{n}^{+}_j$, Equation 2.37 is written:

$$\int_{\Gamma} \hat{n}^{+}_j \left(\tilde{\alpha}^{+}_i - \tilde{\alpha}^{-}_i\right) \mathrm{d}\Gamma = 0_{ij} \tag{2.38}$$

whereby the correct average rotation gradient is obtained.

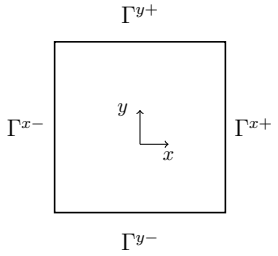

Figure 2.8: Boundaries of the RVE.

Multi point constraints

Multi Point Constraints (MPC) is a feature used in FE-softwares to connect different nodes and degrees of freedom in an analysis. In strain controlled PBC, the displacement is applied using MPC by assigning a displacement-difference between opposite boundaries, as:

$$u_i(\underline{x}^-) - u_i(\underline{x}^+) = \bar{H}_{ij}(x^-_j - x^+_j) + w^-_i - w^+_i \tag{2.39}$$

Assuming the same fluctuation on opposite boundaries, 2.39 is used to express the fluctuation difference as:

$$w^-_i - w^+_i = u_i(\underline{x}^-) - u_i(\underline{x}^+) - \bar{H}_{ij}(x^-_j - x^+_j) = 0_i \tag{2.40}$$

For example, a tension test in pure x-direction with a prescribed x-displacement u_1 and zero y-displacement $u_2 = 0$ at Γ_x, would mean that only $\bar{H}_{11} \neq 0$. The boundary conditions then look like:

$$\begin{aligned} & u_1(\underline{x}^-) - u_1(\underline{x}^+) - \bar{H}_{11}(x_1^- - x_1^+) - \bar{H}_{12}\underbrace{(x_2^- - x_2^+)}_{=0} = \\ & = u_1(\underline{x}^-) - u_1(\underline{x}^+) - \bar{H}_{11}(\underbrace{x_1^-}_{-\frac{L_x}{2}} - \underbrace{x_1^+}_{\frac{L_x}{2}}) = \\ & = u_1(\underline{x}^-) - u_1(\underline{x}^+) + \bar{H}_{11}L_x \end{aligned} \tag{2.41}$$

and in a similar way for u_2:

$$u_2(\underline{x}^-) - u_2(\underline{x}^+) - \bar{H}_{12}(\underbrace{x_2^- - x_2^+}_{=0}) - \underbrace{\bar{H}_{21}}_{=0}(x_1^- - x_1^+) = 0 \tag{2.42}$$

The boundary conditions in Equation 2.41 and 2.42 sums up to:

$$\begin{cases} u_1(\underline{x}^-) - u_1(\underline{x}^+) + \bar{H}_{11}L_x = & 0 \\ u_2(\underline{x}^-) - u_2(\underline{x}^+) = & 0 \end{cases} \tag{2.43}$$

where $\bar{H}_{11}L_x$ represents the applied displacement.

3 Embossed Sheet Model

This chapter presents the methods used to create the embossed sheet model from which the virtual material properties will be identified using FEA. It includes both geometry and surface density aspects, but also the method of finding an accurate RVE size and boundary conditions.

3.1 Embossed geometry

Two different ways to model the embossed geometry were evaluated. The first one was based on 3D-scans provided by Volvo Cars and the other one was mathematically modelled. The coordinate system used for all embossed geometries is defined from the heat shield's global coordinate system shown in Figure 1.1. The pattern running parallel to the global x-direction is defined also as the pattern's x-direction, see Figure 3.1. When different rotations of the pattern around the z-axis are discussed later in the report, this coordinate system indicates the starting position defined as the 0° rotation.

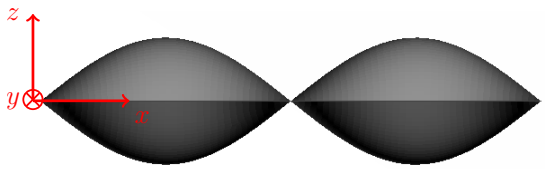

Figure 3.1: The coordinate system used for the embossed structures.

3.1.1 Scanned model

The reference geometry provided by Volvo Cars consisted of 3D-scanned CAD-models in three different sheet thicknesses t; 0.4, 0.6 and 0.7 mm. Figure 3.2 shows an example of how a scanned sheet looks like.

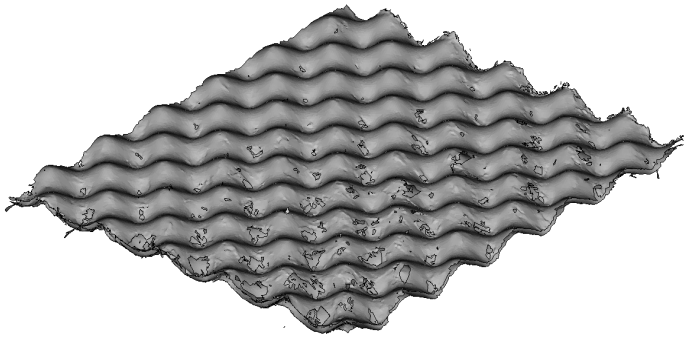

Figure 3.2: 3D-scanned CAD-model of the embossed sheet.

Most relevant for Volvo Cars was the 0.4 and 0.6 mm sheets, hence these were evaluated. Apart from the thicknesses, the embossed sheet's amplitude, A, and wavelength in length and width, a and b respectively, differed for the different sheets. Figure 3.3 illustrates the geometrical parameters on a cross-section of the sheet while Table 3.1 presents the scans' properties where G4 corresponds to the 0.4 mm structure and G6 to the 0.6 mm structure. Here, A, a and b are mean values based on measurements of the scanned model, while t is the nominal value.

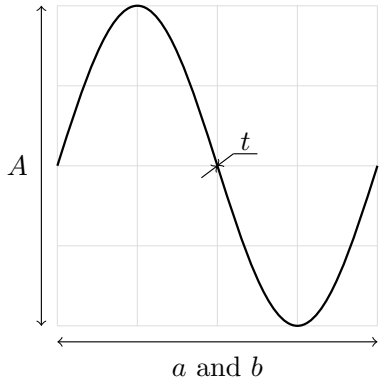

Figure 3.3: Embossed cross-section showing the amplitude A, the thickness t and the wavelengths a and b.

	t [mm]	A [mm]	a [mm]	b [mm]
Geometry G4	0.4	1.79	8.15	7.23
Geometry G6	0.6	1.87	8.09	7.41

Table 3.1: Geometrical parameter data for geometry G4 and G6.

To use the scanned geometries in FE-simulations they needed to be cleaned-up and cut to suitable RVE sizes. However, a couple of aspects made them problematic to use in further analysis.

- The scanned geometries were specimens that had been used in bending tests. Hence, many of the geometries had an initial bent shape.
- The scans had a lot of imperfections making their wavelengths and amplitudes slightly varying. As a result, it was not possible to create cuts exactly between two wavelengths when sizing the RVEs.

3.1.2 Mathematical model

To eliminate the problems mentioned in the previous section, a mathematical model of the embossed geometry was created. The mean surface coordinate, z, was defined by the following mathematical expression:

$$z = \frac{A}{2}\Big(\sin(\frac{2\pi}{a}x) \cdot \sin(\frac{2\pi}{b}y)\Big) \tag{3.1}$$

Surfaces were then created in Matlab and imported into ANSA, see Figure 3.4. Two different geometries were created, one for G4 and one for G6, defined from Table 3.1. A comparison between the mathematical model and the extracted coordinates from the G6 geometry can be seen in Figures 3.5 and 3.6.

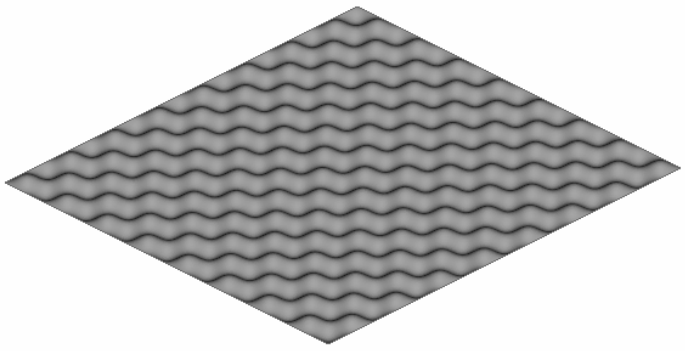

Figure 3.4: Mathematical model of the embossed sheet.

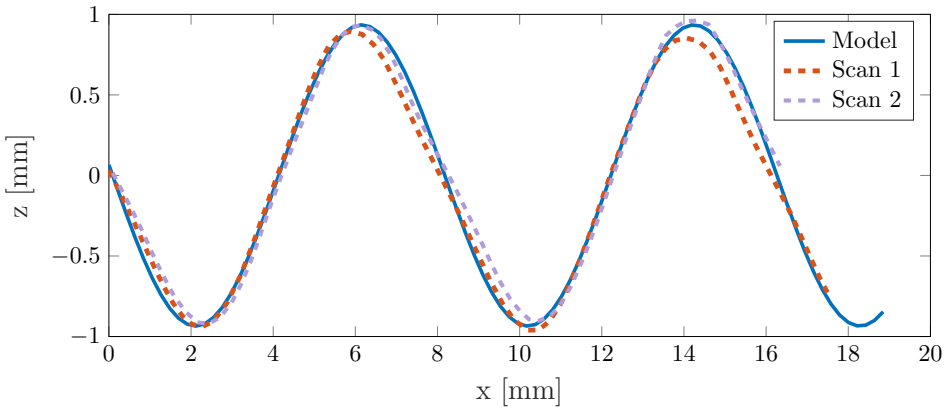

Figure 3.5: Comparison between the mathematical model and x-coordinates extracted from the scan.

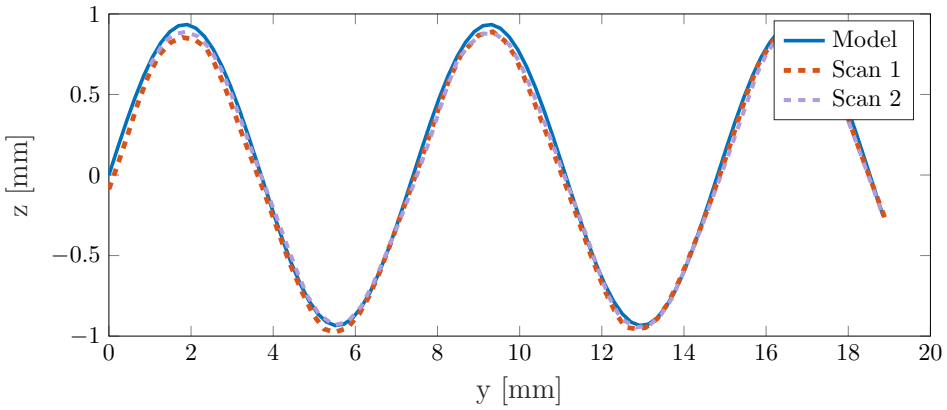

Figure 3.6: Comparison between the mathematical model and y-coordinates extracted from the scan.

3.1.3 Results: model validation

To verify that the mathematical model could represent the scanned geometry, simulations that compared their response in pure bending, pure tension and pure shear were conducted. DBC were used with a mesh size of 0.1mm. The tests were done on equally sized rectangles with an equal number of wavelengths in each direction. Three versions of the same geometries were created from the scanned sheets to take potential imperfections between different samples into account. Figure 3.7 shows the result for the different loadings. Geometry G6 has been used for the validation.

The graphs show that the mathematical model follows the behaviour of the scans in all three loading scenarios. In some regions the values differ slightly, both between the mathematical model and the scans, but also between the different versions of the same scan. This can be explained due to the inconsistency of the scanned geometry. However, the mathematical model approximate the scanned geometries well, and will be used in all further simulations in this work.

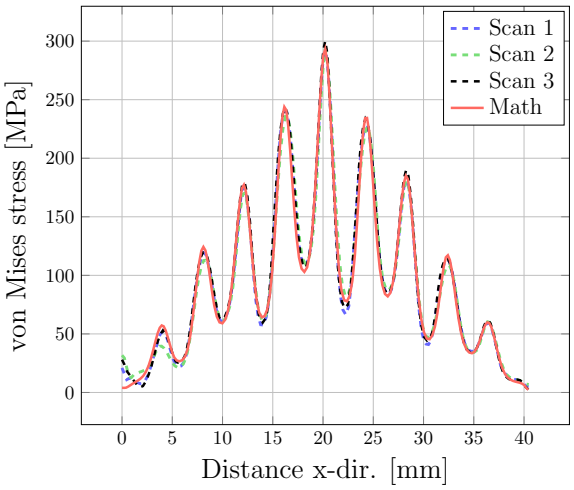

(a) von Mises stress in bending.

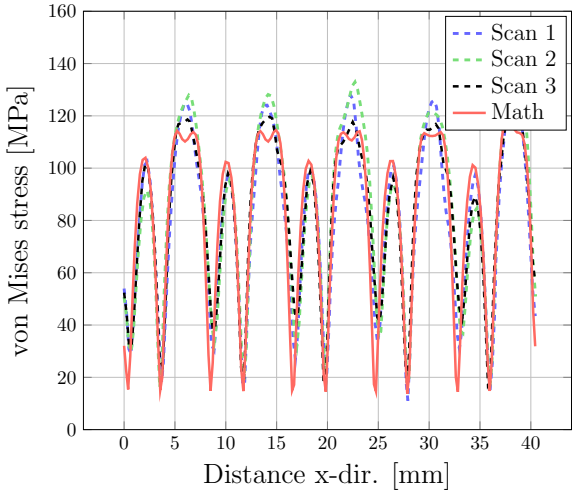

(b) von Mises stress in tension.

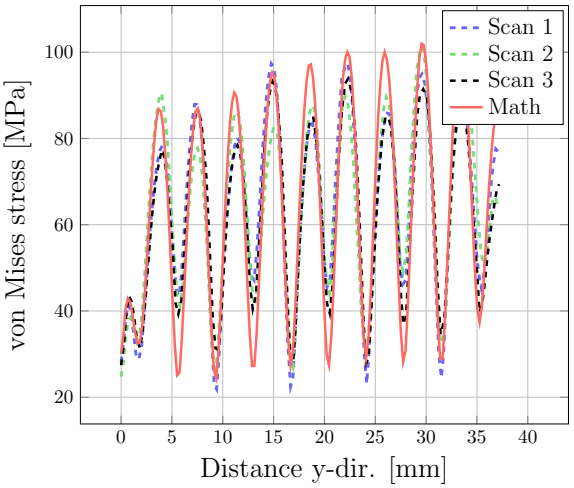

(c) von Mises stress in shear.

Figure 3.7: Graphs comparing the behaviours of the scanned geometry and the mathematical model.

3.2 Surface density

The surface density ρ_A is defined as the density ρ times the thickness t. For aluminium with a density of $\rho = 2.70$ g/cm^3, the surface density becomes:

$$\rho_A^{Al} = \rho t = 2.7\, t \quad \text{g/cm}^2 \tag{3.2}$$

The embossed pattern of the sheet causes the surface area A_{emb} to increase compared to a flat sheet with surface area A_{flat}. Because of this, the surface density needs to be adjusted in the virtual material. The mass for an embossed sheet with aluminium as material should equal the mass for a flat sheet with the virtual material's surface density. Hence, ρ_A^{vm} can be calculated by:

$$\rho_A^{Al} A_{emb} = \rho_A^{vm} A_{flat} \quad \Rightarrow \quad \rho_A^{vm} = \rho_A^{Al} \frac{A_{emb}}{A_{flat}} \tag{3.3}$$

Here, A_{emb} is the area of the embossed sheet, measured on the mathematical model, and A_{flat} is the area for an equally large flat sheet. The results for geometry G4 and G6 are given in Table 3.2.

	A_{flat} [cm^2]	A_{emb} [cm^2]	ρ_A^{Al} [g/cm^2]	ρ_A^{vm} [g/cm^2]	increase [%]
G4	0.589	0.663	0.108	0.122	13.0
G6	0.599	0.679	0.162	0.184	13.6

Table 3.2: Surface density data for geometry G4 and G6.

3.3 Boundary condition implementation

This section describes how the DBC and PBC, described in Section 2.3, are implemented in Abaqus for the virtual tests.

3.3.1 Dirichlet Boundary Conditions

The notation used for boundaries and corners are as illustrated in Figure 3.8. Table 3.3 describes the DBC for a tension test in the x-direction, an applied ϵ_{xx}. The numbers 1 to 6 represent the six degrees of freedom. A value 0 denotes that the edge/node is fixed and *free* denotes that it is free to move in that degree of freedom. A simular approach was used for the applied ϵ_{yy}. The settings for the shear test with an applied ϵ_{xy} can be found in Appendix E.

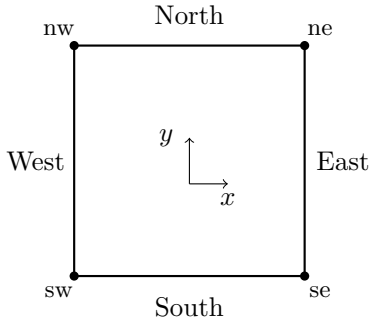

Figure 3.8: Edges and nodes of the RVE.

	→ 1	→ 2	→ 3	↺ 4	↺ 5	↺ 6
West	-$u_x^0/2$	0	free	0	0	free
East	$u_x^0/2$	0	free	0	0	free
North	free	0	free	0	0	free
South	free	0	free	0	0	free
nw	-$u_x^0/2$	0	free	0	0	free
sw	-$u_x^0/2$	0	free	0	0	free
ne	$u_x^0/2$	0	free	0	0	free
se	$u_x^0/2$	0	free	0	0	free

Table 3.3: Symmetric Dirichlet boundary conditions for $\bar{\epsilon}_{xx}$.

In the same way, the bending test with applied curvature κ_{xx} was implemented, see Table 3.4. The test for κ_{yy} was created similarly while the twisting test with an applied κ_{xy} needed slightly different conditions. These are described further in Appendix E.

	→ 1	→ 2	→ 3	↺ 4	↺ 5	↺ 6
West	0	0	free	0	$-\alpha_y/2$	free
East	0	0	free	0	$\alpha_y/2$	free
North	0	0	free	0	free	free
South	0	0	free	0	free	free
nw	0	0	free	0	$-\alpha_y/2$	free
sw	0	0	free	0	$-\alpha_y/2$	free
ne	0	0	free	0	$\alpha_y/2$	free
se	0	0	free	0	$\alpha_y/2$	free

Table 3.4: Dirichlet boundary conditions for $\bar{\kappa}_{xx}$.

Note that these are simplified DBC. The north and south boundaries at degree of freedom 1 in Table 3.3 are free. But they should in fact also be prescribed as $u_x^0 x/2L_x$. The same is true for the north and south boundary at degree of freedom 5 in Table 3.4, where they should be prescribed as $\alpha_y x/2L_x$. This is done to simplify the implementation.

3.3.2 Periodic boundary conditions

Strain controlled PBC are implemented in Abaqus using MPC with the keyword **Equation*. The applied strain is achieved by assigning a difference in displacement between opposite boundaries of the RVE. The general form of the MPC is given as:

$$A_1 u_i^P + A_2 u_j^Q + ... + A_N u_k^R = 0 \tag{3.4}$$

Here, u is the given displacement at node or node set $P, Q...R$ in degree of freedom $i, j...k$ and $A_1, A_2...A_N$ are the coefficients that controls the nodes' relative motions [16]. An example of how this is implemented in an Abaqus input file is found below [9]:

```
*Equation
3 #Define an equation with 3 terms
P, i, A1, Q, j, A2, R, k, A3.
```

To further illustrate, the first row in Equation 3.5 was implemented as follows. The A-values are defined as 1 and -1, meaning that the applied displacement is equal but takes opposite signs at opposite boundaries. Due to limitations in **Equation*, all MPC must equal zero. In order to assign a displacement difference, an arbitrary dummy node is introduced. The displacement is applied on the dummy node, $u_{dummy} = value$, and its motion is transferred to the boundaries through the MPC. The applied displacement on the dummy node is corresponding to $\bar{H}_{ij}L$ in Equation 2.43.

```
*Equation
3
Set-west, 1, 1, Set-east, 1, -1. Dummy, 1, 1.
#West and east set is constrained to a dummy node in DOF 1, in opposite directions
```

PBC also require some special attributes on the finite element mesh. Since MPC connect nodes at opposite boundaries of the RVE, the mesh should be periodic. Also, Abaqus connects the nodes depending on the node numbering, which makes this something crucial to define. Referring to Figure 3.8, the west and east boundary must have their lowest node number at the southernmost node, and their highest at the northernmost. The same goes for the north and south boundaries, where node numbering instead needs to go from west to east.

For the virtual tensile test in x-direction, the edge MPC were defined as in Equation 3.5 and corner MPC as in Equation 3.6. Important to note is that the corners were coupled diagonal-wise [17]. The PBC for the tension

in y-direction were defined similarly. The conditions for the shear test can be found in Appendix B.

$$\begin{aligned} u_x^{West} - u_x^{East} - u_{x,dummy} &= 0 \\ u_x^{South} - u_x^{North} &= 0 \\ u_y^{West} - u_y^{East} &= 0 \\ u_y^{South} - u_y^{North} &= 0 \\ \alpha_x^{West} - \alpha_x^{East} &= 0 \\ \alpha_x^{South} - \alpha_x^{North} &= 0 \\ \alpha_y^{West} - \alpha_y^{East} &= 0 \\ \alpha_y^{South} - \alpha_y^{North} &= 0 \end{aligned} \tag{3.5}$$

$$\begin{aligned} u_x^{nw} - u_x^{se} - u_{x,dummy} &= 0 \\ u_x^{sw} - u_x^{ne} - u_{x,dummy} &= 0 \\ u_y^{nw} - u_y^{se} &= 0 \\ u_y^{sw} - u_y^{ne} &= 0 \end{aligned} \tag{3.6}$$

3.3.3 Results: boundary condition validation and RVE size study

The two types of boundary conditions were tested to identify differences in the results for different Volume Element (VE) sizes to identify the appropriate RVE size. The variable of interest was the area averaged stress $\underline{\bar{\sigma}}$ defined as:

$$\underline{\bar{\sigma}} = \frac{1}{A} \int_\Omega \underline{\sigma} \, \mathrm{d}\Omega \tag{3.7}$$

Here, Ω denotes the domain and A its area. Two tensile test were conducted; one test with tension in the x-direction and one in shear in the xy-plane. The corresponding stresses dominant for each test were $\bar{\sigma}_{xx}$ and $\bar{\sigma}_{xy}$ respectively, why these values were of interest. The size of the VE spanned from one wavelength in each direction to eight wavelengths in each direction. The results can be seen in Figures 3.9 and 3.10.

For a sufficiently large domain, about 8 wavelengths in each directions, both types of boundary conditions give approximately the same result. The difference is how fast they converge. The PBC converge already for the smallest VE size of one wavelength, while the DBC require about eight wavelengths to reach the same values. This is due to the PBC ability to minimise boundary effects. For small VE sizes, boundary effects of the DBC are still significant. It should be noted however that for the tension test the error with the DBC was below 1% for the smallest VE size.

Similar tests for the DBC were conducted in bending. Figure 3.11 shows the reaction moments $\bar{M}_{xx}$ for a $\bar{\kappa}_{xx}$ bending test and 3.11 shows $\bar{M}_{xy}$ for a $\bar{\kappa}_{xy}$ twisting test. The DBC showed the same behaviour as in tension, a convergence with an VE size of 8 wavelengths. It was concluded that this was the size for which the VE became an RVE.

Since the DBC gave the same results as the PBC, with a reasonable VE size that still was not computationally heavy, it was chosen to proceed with DBC because of its ease of implementation. This meant that an RVE with the size of 8 wavelengths in the x- and y-directions was established.

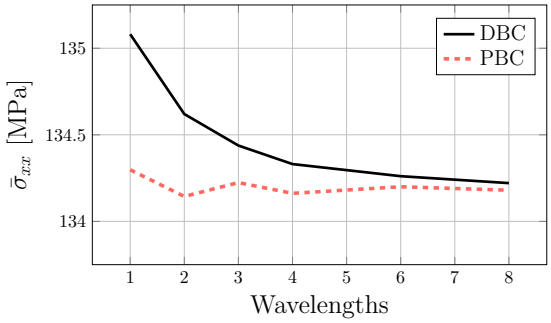

Figure 3.9: Size study and boundary condition comparison for tension test $\bar{\epsilon}^0_{xx}$.

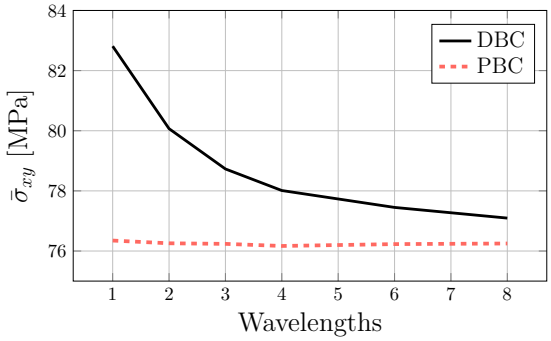

Figure 3.10: Size study and boundary condition comparison for shear test $\bar{\epsilon}^0_{xy}$.

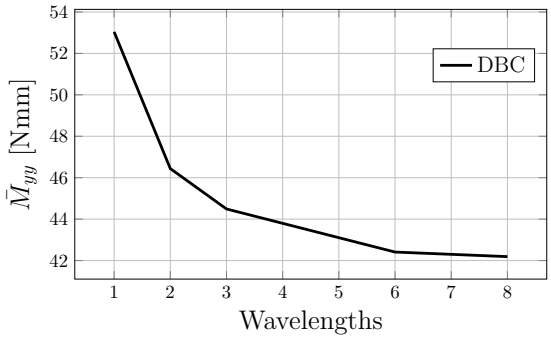

Figure 3.11: Size study for bending test $\bar{\kappa}_{xx}$.

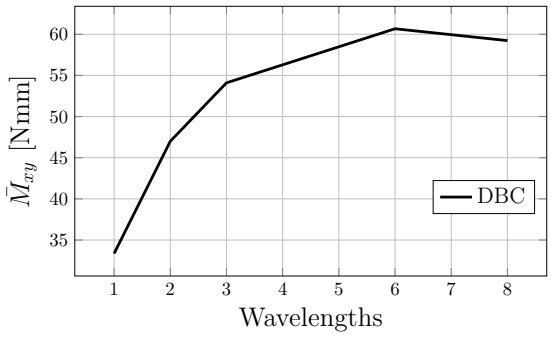

Figure 3.12: Size study for twisting test $\bar{\kappa}_{xy}$.

4 Homogenisation

This chapter present the homogenisation of the embossed aluminium sheets. It explains the method for virtual material testing and the FEA set-up. It also presents the homogenisation results and a method for implementing the virtual material model in Abaqus.

4.1 Method: virtual material testing

The following section describes the homogenisation procedure starting with the method for the virtual tests in tension and bending followed by the set-up for the FE analyses.

4.1.1 Tensile and bending test setup

To find the tensile and bending properties, six different tests were conducted as shown in Figures 4.1 and 4.2. Out of these tests, two are in elongation and one in shear, followed by two tests in bending and one in twisting.

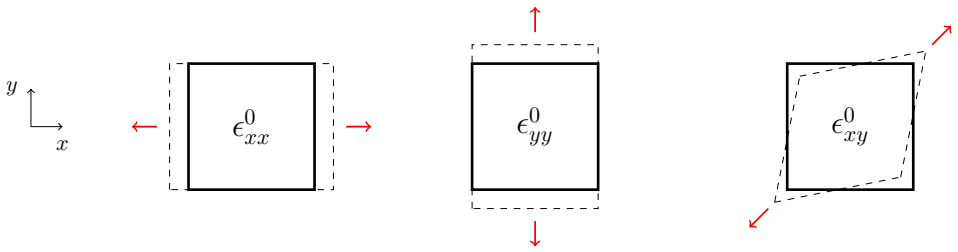

Figure 4.1: Virtual material testing: tension and shear.

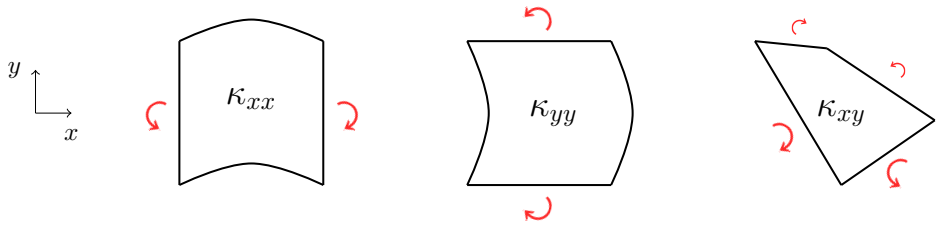

Figure 4.2: Virtual material testing: bending and twisting.

The loading scenarios were simulated by controlling the boundary conditions in $\underline{\epsilon}^0$ and $\underline{\kappa}$. For the tensile tests, $\underline{\epsilon}^0$ were induced by applying displacements along either the x- or y-direction. The bending test were done by applying rotations around the x- or y-axis to simulate $\underline{\kappa}$.

The simulation output in terms of macroscopic reaction forces $\underline{\bar{N}}$ and reaction moments $\underline{\bar{M}}$, were calculated as the average of reaction forces and moments N and M over the boundaries Γ^+:

$$\begin{aligned} \underline{\bar{N}} &= \frac{1}{L}\int_{\Gamma^+} \underline{N}\,\mathrm{d}\Gamma \\ \underline{\bar{M}} &= \frac{1}{L}\int_{\Gamma^+} \underline{M}\,\mathrm{d}\Gamma \end{aligned} \tag{4.1}$$

Here, L corresponds to the RVE lengths presented in Figure 2.2. As an example, the normal force in x-direction was calculated as:

$$\underline{\bar{N}}_{xx} = \frac{1}{L_y}\int_{-L_y}^{L_y} \underline{N}_{xx}(L_x/2, y)\,\mathrm{d}y = \frac{1}{L_y}\sum_{\Gamma^+} \underline{N}_{xx} \tag{4.2}$$

The other reaction quantities were calculated in the same way. Note that the twisting moments in different directions were not necessarily equal, $M_{xy} \neq M_{yx}$. Instead the average twisting moment was used, $M_{av} = \frac{1}{2}(M_{xy} + M_{yx})$ [18].

Now the stiffness matrices $\underline{A}$, $\underline{B}$ and $\underline{D}$ could be identified using Equation 2.15. An example is given below for the first test where an elongation in the x-direction, $\bar{\epsilon}^0_{xx}$, is applied to the RVE while prescribing $\bar{\epsilon}^0_{yy} = 2\bar{\epsilon}^0_{xy} = \bar{\kappa}_{xx} = \bar{\kappa}_{yy} = 2\bar{\kappa}_{xy} = 0$. This gives Equation 4.3 which shows that the first column of the $\underline{A}$ and $\underline{B}$ matrices can be identified. Doing this for all six virtual tests gives the complete stiffness matrices.

$$\begin{aligned}
\underline{\bar{N}}_{xx} &= A_{11}\bar{\epsilon}^0_{xx} \\
\underline{\bar{N}}_{yy} &= A_{12}\bar{\epsilon}^0_{yy} \\
\underline{\bar{N}}_{xy} &= A_{16}\bar{\epsilon}^0_{xy} \\
\underline{\bar{M}}_{xx} &= B_{11}\bar{\kappa}^0_{xx} \\
\underline{\bar{M}}_{yy} &= B_{12}\bar{\kappa}^0_{yy} \\
\underline{\bar{M}}_{av} &= B_{16}\bar{\kappa}^0_{xy}
\end{aligned} \tag{4.3}$$

4.1.2 Loading

Throughout the homogenisation analysis the same loading conditions were used. For the tensile tests, a mid-plane strain of $\bar{\epsilon}^0 = 0.025$ was used, which corresponds to an applied displacement of $u^0 = \bar{\epsilon}^0 L$. In the bending tests, a rotation of $\bar{\alpha} = 0.03$ radians was applied. The particular values were chosen so that the structural response was kept within the elastic region, thus the von Mises stress is below the yield limit, $\sigma^{vm} < \sigma_y^{Al}$.

4.1.3 Mesh

The FE-mesh consists of first order quadrilateral 4-node shell elements, see Figure 4.3. To make sure that the simulation results were independent of the mesh size, a mesh convergence study was conducted. Figure 4.4 shows the results of the mesh convergence studies for a VE size of one wavelength for three different loading cases with DBC. In the results, $\bar{\sigma}_{xx}$ represents data from a tensile test in x-direction, $\bar{\sigma}_{xy}$ data from a shear test and $\bar{M}_{yy}$ data for a bending test.

All quantities converged around the same mesh density; about 7000 elements corresponding to a cell size of 0.1 mm. This study was done in parallel to the size study of the VE, why all sizes have their own mesh studies. However, all VE sizes showed similar behaviour and converged around the cell size 0.1 mm. Hence, this mesh size was assumed valid throughout the rest of the thesis.

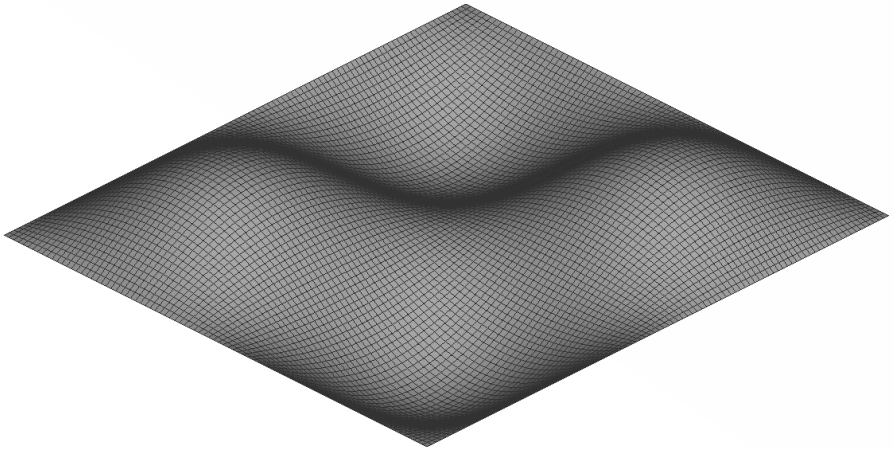

Figure 4.3: Quadrilateral shell element mesh with size 0.1 mm for a 1 wavelength VE.

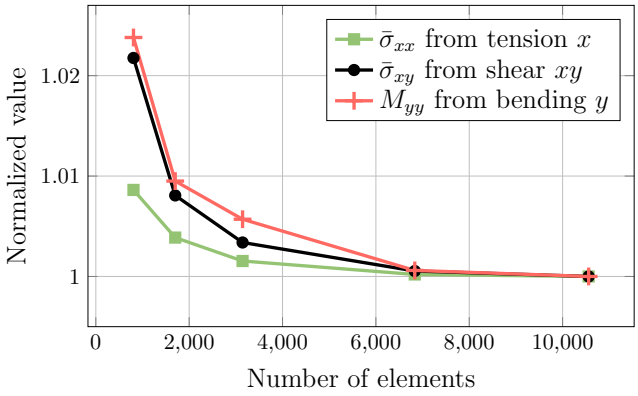

Figure 4.4: Mesh convergence study for a 1 wavelength VE.

4.1.4 Material

The material used in the embossing process was *Aluminium EN 485-2 AW-1050A* with the properties shown in Table 4.1. This material was used in the virtual tests of the embossed structure and also when modelling the flat aluminium sheet used as reference during the verification process.

	E [GPa]	ν [-]	G [GPa]	ρ [g/cm^3]
Al 99.5 EN-AW 1050	69	0.33	26	2.70

Table 4.1: Material parameter data for Al 99.5 EN-AW 1050.

4.2 Results: virtual material model

The results for the virtual material testing are presented in terms of the tensile and bending behaviours for the G4 and G6 geometries. The orthotropic behaviour is investigated as well as the effects of the $\underline{B}$-matrix and the asymmetry of $\underline{A}$ and $\underline{D}$. Figures 4.5 and 4.6 show the deformation modes on the RVE in the six virtual tests. The displacements are scaled with a factor 10.

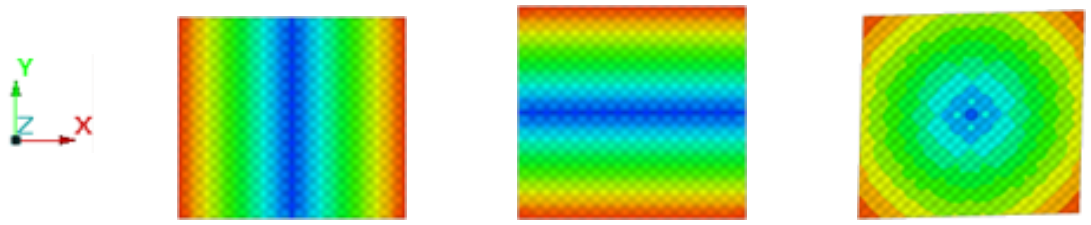

(a) Applied $\bar{\epsilon}^0_{xx}$. (b) Applied $\bar{\epsilon}^0_{yy}$. (c) Applied $\bar{\epsilon}^0_{xy}$.

Figure 4.5: Deformation modes for the RVE during the virtual material testing in tension and shear.

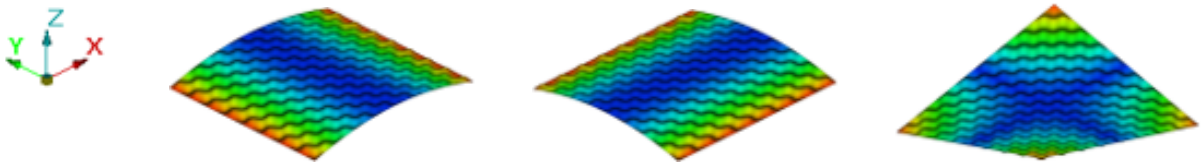

(a) Applied $\bar{\kappa}_{xx}$. (b) Applied $\bar{\kappa}_{yy}$. (c) Applied $\bar{\kappa}_{xy}$.

Figure 4.6: Deformation modes for the RVE during the virtual material testing in bending and twisting.

4.2.1 Tensile and bending behaviour

The result of the virtual material testing for geometry G4 and G6 in terms of the $\underline{A}$ and $\underline{D}$ matrices are given in Equations 4.4 and 4.5. The coupling matrices $\underline{B}^{G4}$ and $\underline{B}^{G6}$ were omitted since their contribution was negligible, this is further discussed in Section 4.2.3, where also the slight asymmetry of $\underline{A}$ and $\underline{B}$ is covered.

$$\underline{A}^{G4} = \begin{bmatrix} 1.636 & -0.236 & 0 \\ -0.241 & 1.346 & 0 \\ 0.000 & 0.000 & 0.196 \end{bmatrix} 10^4 \ \frac{\text{N}}{\text{mm}} \quad \underline{D}^{G4} = \begin{bmatrix} 0.812 & 0.353 & 0 \\ 0.360 & 0.673 & 0 \\ -0.001 & 0.000 & 1.042 \end{bmatrix} 10^3 \ \text{Nmm} \tag{4.4}$$

$$\underline{A}^{G6} = \begin{bmatrix} 2.542 & -0.225 & 0 \\ -0.231 & 2.243 & 0 \\ 0.000 & 0.000 & 0.488 \end{bmatrix} 10^4 \ \frac{\text{N}}{\text{mm}} \quad \underline{D}^{G6} = \begin{bmatrix} 2.302 & 1.012 & 0 \\ 1.019 & 2.052 & 0 \\ -0.001 & 0.001 & 1.907 \end{bmatrix} 10^3 \ \text{Nmm} \tag{4.5}$$

By using the least squares method [19] and the nonlinear simplex solver *fminsearch* in Matlab [20], the values in the $\underline{A}$ and $\underline{D}$ matrices were optimised to Equations 2.17 and 2.19. This enabled the results to be expressed in terms of the elastic modulus E, shear modulus G and Poisson's ratios ν for the tensile and bending behaviours respectively, see Tables 4.2 and 4.3. As mentioned earlier, the virtual material can also be seen as a *virtual structure*, so these values are specific to certain thicknesses and geometries, and describe the relative behaviour in comparison with a flat aluminium sheet. For example, the larger value of G^D_{xy} for G4 does not necessarily mean that it is stiffer than G6, but rather that the embossed pattern has a greater impact on the thinner geometry.

	E_x [GPa]	E_y [GPa]	ν_{xy} [-]	ν_{yx} [-]	G_{xy} [GPa]
Reference aluminium	69	69	0.33	0.33	26
Tensile behaviour	39.84	32.78	-0.175	-0.147	4.90
Bending behaviour	116.80	96.84	0.525	0.443	195.40

Table 4.2: Relative material properties for geometry G4.

	E_x [GPa]	E_y [GPa]	ν_{xy} [-]	ν_{yx} [-]	G_{xy} [GPa]
Reference aluminium	69	69	0.33	0.33	26
Tensile behaviour	41.98	37.04	-0.103	-0.092	8.13
Bending behaviour	99.96	89.12	0.492	0.441	106.01

Table 4.3: Relative material properties for geometry G6.

It is noted that the virtual material of the embossed sheet has a larger bending stiffness in comparison with isotropic aluminium. In tension however, the virtual material displays a less stiff behaviour compared to isotropic aluminium. The reason for this is explained by the pattern-stretch effect, where the embossed pattern is stretched out when subjected to tensile loads. This requires less force compared to elongating the material.

Another interesting characteristics of the embossed sheet are the negative Poison's ratios, ν_{xy} and ν_{yx}. This means that the pattern, when subjected to pure tension in x-direction, will expand in the y-direction. This is once again explained by the pattern-stretch effect.

4.2.2 Level of anisotropy

To evaluate how the virtual material behaves in different directions, the material properties E_x, E_y and G_{xy} are plotted with respect to angle θ around the out-of-plane axis z. The xy-coordinate system used to derive material the model from previous sections represents 0°. For geometry G6 Figure 4.7 shows the tensile behaviour, E^A and G^A, and Figure 4.8 the bending behaviour, E^D and G^D. All values are normalised with the value of isotropic aluminium, which also is plotted as references. Similar plots for G4 are found in Appendix F.

The results clearly show the orthotropic behaviour. It also shows that in tension (Figure 4.7), the virtual material is more flexible than aluminium and that E_x^A and E_y^A are stiffest in 0°/90°, while G_{xy}^A is stiffest in 45°. In bending however (Figure 4.8), the virtual material model is stiffer than aluminium. Here, E_x^D and E_y^D are stiffest in 45° while G_{xy}^A are significantly more stiff in 0/90°.

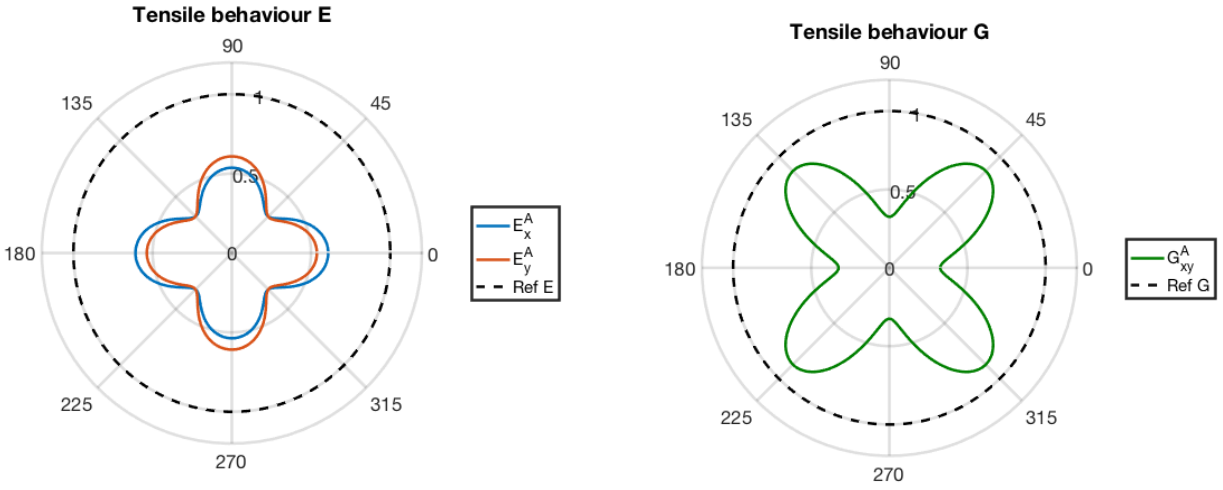

Figure 4.7: Normalised in-plane modulus and shear modulus tensile behaviour for geometry G6.

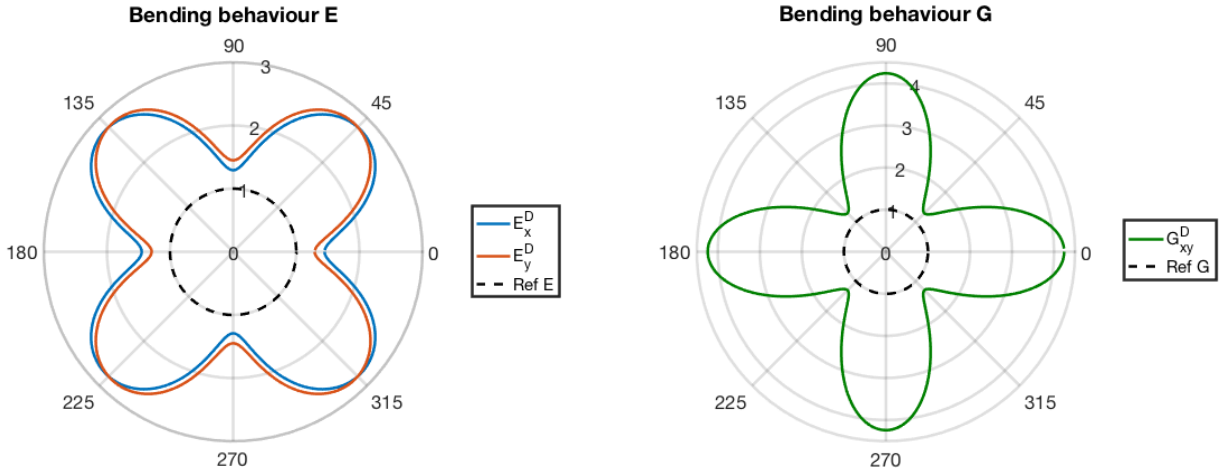

Figure 4.8: Normalised in-plane modulus and shear modulus bending behaviour for geometry G6.

4.2.3 Effect of B-matrix and asymmetry

In addition to the $\underline{A}$ and $\underline{D}$ matrices, Equation 4.6 presents the $\underline{B}$-matrices for geometry G6. The values in the $\underline{B}^A$ matrix come from the tensile test and the ones in the $\underline{B}^D$ matrix come from the bending tests. Since the implementation method in Abaqus, *Shell general section*, only can handle one $\underline{B}$-matrix it would be beneficial if $\underline{B}$ had small influence on the results.

$$\underline{B}^A = \begin{bmatrix} 4.118 & 1.043 & -29.593 \\ 0.387 & 0.232 & 31.876 \\ -72.709 & -75.998 & 0.433 \end{bmatrix} \text{N} \quad \underline{B}^D = \begin{bmatrix} 0.153 & 0.189 & -111.665 \\ 0.049 & 0.171 & -100.214 \\ 121.720 & -119.608 & 0.590 \end{bmatrix} \text{N} \tag{4.6}$$

To investigate their effect on the embossed structure, the corner bending test from Section 5.1.2 and the modal analysis from Section 5.2.2 were conducted with the two different $\underline{B}$-matrices and a test with $\underline{B} = \underline{0}$. The results are given in Table 4.5 where the normalised maximum displacement is presented and in Table 4.4 where the first two normalised natural frequencies are presented. All values are normalised with the value for $B = 0$.

The difference is negligible and hence it was decided to omit the $\underline{B}$-matrix from future simulations and assume no coupling, i.e. $\underline{B} = \underline{0}$.

	Max. disp. [-]
$\underline{B} = \underline{B}^A$	1.0000029
$\underline{B} = \underline{B}^D$	1.00062
$\underline{B} = \underline{0}$	1

Table 4.4: Effect of $\underline{B}$-matrix on the normalised maximum displacement in a corner bending test.

	1st mode	2nd mode
$\underline{B} = \underline{B}^A$	1.00055	1.00034
$\underline{B} = \underline{B}^D$	0.997	0.998
$\underline{B} = \underline{0}$	1	1

Table 4.5: Effect of $\underline{B}$-matrix on the normalised natural frequencies in a modal analysis.

The $\underline{A}$ and $\underline{D}$ matrices were also slightly asymmetric, $A_{21} \neq A_{12}$ etc. Once again, since the implementation method in Abaqus required symmetrical matrices it would be beneficial if the effect of their asymmetry was negligible. It was tested similarly to the asymmetric $\underline{B}$-matrix effect, with results shown in Table 4.6. Here, the upper symmetry is referring to the values visible in Equation 4.7 and lower symmetry to the values in the lower region including the ones along the diagonal. As the table shows, the asymmetric effect is negligible, so in future simulations only the upper symmetry will be used.

	Max. disp. [mm]
Upper symmetry	1.019895
Lower symmetry	1.019893

Table 4.6: Effect of asymmetric A and D matrices in a corner bending test.

4.3 Implementation of virtual material model

The virtual material model can be implemented in Abaqus using the command **Shell general section*, which allows the matrices $\underline{A}$, $\underline{B}$ and $\underline{D}$ to be specified directly. No other material definitions nor thickness input is required. The matrices are defined in the form:

$$\begin{bmatrix} A_{11} & A_{12} & A_{13} & B_{11} & B_{12} & B_{13} \\ & A_{22} & A_{23} & B_{21} & B_{22} & B_{23} \\ & & A_{33} & B_{31} & B_{32} & B_{33} \\ & & & D_{11} & D_{21} & D_{31} \\ & \text{sym} & & & D_{22} & D_{23} \\ & & & & & D_{33} \end{bmatrix} \tag{4.7}$$

In the Abaqus input file, the values are specified column-wise according to [9]:

```
*SHELL GENERAL SECTION, ELSET=elements, DENSITY=surface_density,ORIENTATION=orientation
A11,A12,A22,A13,A23,A33,B11,B21
B31,D11,B12,B22,B32,D12,D22,B13
B23,B33,D13,D23,D33
```

Important to note is that the defined density is the surface density, so that it becomes independent of thickness. The material direction can also be specified.

4.3.1 Alternative methods

An alternative way to implement the virtual material model might be to using MSC Nastran that allows material input in terms of tensile and bending parameters. Another way, that could be independent of software, is if the virtual material was modelled as a laminate where the material properties in tension and bending were represented in different layers. A schematic of the laminate method is illustrated in Figure 4.9. However, none of these methods was evaluated in this thesis.

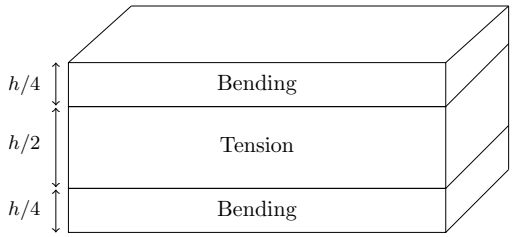

Figure 4.9: Laminate method.

5 Verification

To verify the virtual material model, a flat specimen with the derived virtual material model was evaluated in tensile, bending and modal analyses. In the first section, a specimen with fully resolved embossed pattern made of aluminium will be used as verification data. In the second section, the virtual material model will be compared to physical test data from [3]. All tests will be compared to a flat non-embossed sheet with corresponding thickness and aluminium as material.

For the tensile and bending verification tests, the results are presented as force-displacement curves. The slopes of these curves can be seen as the relative stiffness for that particular loading scenario. The steeper the slope the stiffer the response from the material. To ease the stiffness comparisons, a normalised reference stiffness k is introduced. k is defined as the slope of the force-displacement curves, normalised with a slope of interest k_{norm}. F is the force and u the displacement.

$$k = \frac{(F_2 - F_1)}{(u_2 - u_1)} \cdot \frac{1}{k_{norm}} \tag{5.1}$$

5.1 FE-verification

The FE-verification consists of one tensile test and one bending test, where the virtual material is compared to a fully resolved embossed sheet. In both analyses, the size of the specimen corresponds to 15x15 wavelengths of the embossed structure and the material direction is 0°.

5.1.1 Tensile test

The tensile verification tests were conducted by applying a force in the x-direction along one of the boundaries, while keeping the opposite boundary fixed in the x-direction. The movement along y is fixed at the lower boundary only and all boundaries are fixed in z-direction. Figure 5.1 illustrates the loading scenario.

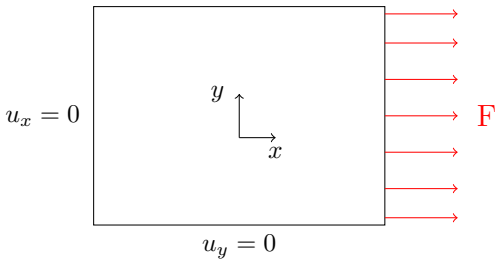

Figure 5.1: Boundary conditions for the tensile verification test.

The results for the sheet thicknesses 0.4 and 0.6 mm corresponding to geometry G4 and G6 are shown in Table 5.1 where the displacement for the maximum load and the reference stiffness k, normalised with the value for the virtual material, are presented. The force-displacement curve is shown in Figure 5.2. The embossed sheet indicates a lower tensile stiffness compared to a flat aluminium sheet. The virtual material model behaves very similar to the fully resolved embossed sheet with only a few percents difference.

	G4		G6	
	Max. disp. [mm]	k [-]	Max. disp. [mm]	k [-]
Virtual material	0.70	1	0.45	1
Embossed sheet	0.71	0.99	0.44	1.02
Flat sheet	0.41	1.74	0.27	1.65

Table 5.1: Result data for the tensile verification test.

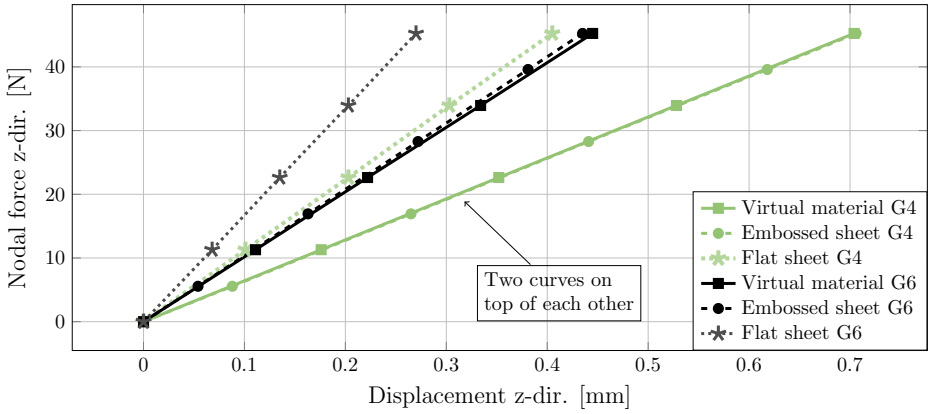

Figure 5.2: Force-displacement curves for the tensile verification test.

5.1.2 Corner bending test

The corner bending test was set-up as a plate, fully fixed along two edges, with a point load applied in the opposite corner, see Figure 5.3.

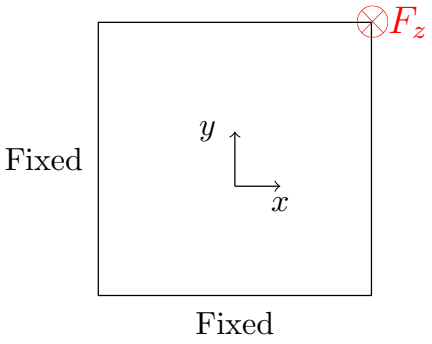

Figure 5.3: Illustration of the set-up for the corner bending test.

The results for geometry G4 and G6 are shown in Table 5.2 and Figure 5.4. In contrast to the tensile behaviour, the embossed sheet is stiffer in bending compared to a flat sheet. The virtual material under-predicts the stiffness compared to the fully resolved embossed sheet for both geometries with 19% respectively 14%. However, the virtual materials behaviour is much closer to the embossed sheet compared to the flat sheet. The effect becomes especially distinct in the thinner geometry G4.

	G4		G6	
	Max. disp. [mm]	k [-]	Max. disp. [mm]	k [-]
Virtual material	2.11	1	1.02	1
Embossed sheet	1.78	1.19	0.89	1.14
Flat sheet	9.77	0.21	2.90	0.35

Table 5.2: Result data for the corner bending test.

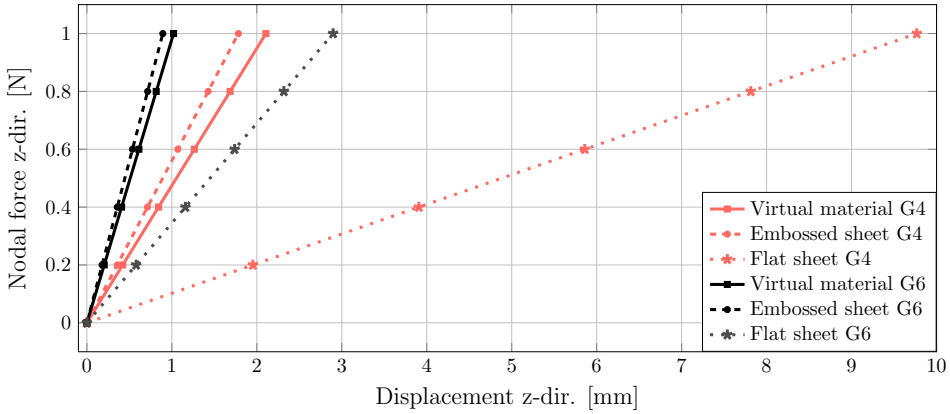

Figure 5.4: Force-displacement curves for the corner bending test.

5.2 Physical data verification

The virtual material model will also be evaluated to physical data from a three point bending test and a modal analysis.

5.2.1 Three point bending test

The three point bending test was conducted to simulate the physical test previously done in [3]. A specimen with length 200mm and width 50mm was used with boundary conditions shown in Figure 5.5. The two roller supports are placed 40 mm from each end. The load was distributed along the width. Three different material direction were tested, 45°, 0° and 90°.

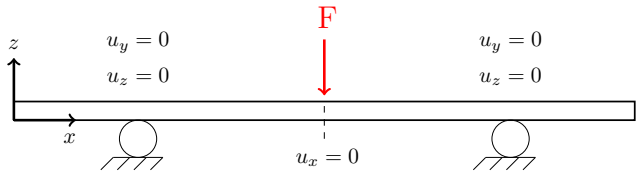

Figure 5.5: Set-up and boundary conditions for the three point bending test.

The results are presented in Table 5.3, where the physical data represents the mean value and the relative stiffness k is normalised with the stiffness of a flat sheet. Figures 5.6 and 5.7 show the force-displacement curves. The physical data from [3] had to be slightly adjusted for the comparison since it had some measurement errors in the first data points. This was assumed to be due to factors such as pre-deformed sheets and contact problems. Hence, the data graphs were translated so that the slope of the linear elastic zone was correct. Note that the displacement axes in the different plots have different scales. For example, the physical data is not more consistent in the G6 geometry even though it might look like this is the case.

The virtual material model significantly overestimates the stiffness in all three material directions for both G4 and G6. This in contrast to the result for the corner bending test, where the virtual model instead underestimated the stiffness compared to the fully resolved embossed sheet. The influence of the material orientation is however well captured. The orientation of 45° was stiffest for both G4 and G6, while 0° and 90° performed similar to a flat sheet in G4, but worse than a flat sheet in G6.

	G4		**G6**	
	Max. disp. [mm]	k [-]	Max. disp. [mm]	k [-]
Virtual material 45°	1.40	4.19	0.61	2.74
Physical data 45°	2.50	2.34	1.10	1.38
Virtual material 0°	3.12	1.88	1.12	1.48
Physical data 0°	2.50	1.07	1.50	0.70
Virtual material 90°	3.66	1.60	1.21	1.37
Physical data 90°	2.50	0.88	1.20	0.59
Flat sheet	5.86	1	1.67	1

Table 5.3: Result data for the three point bending test.

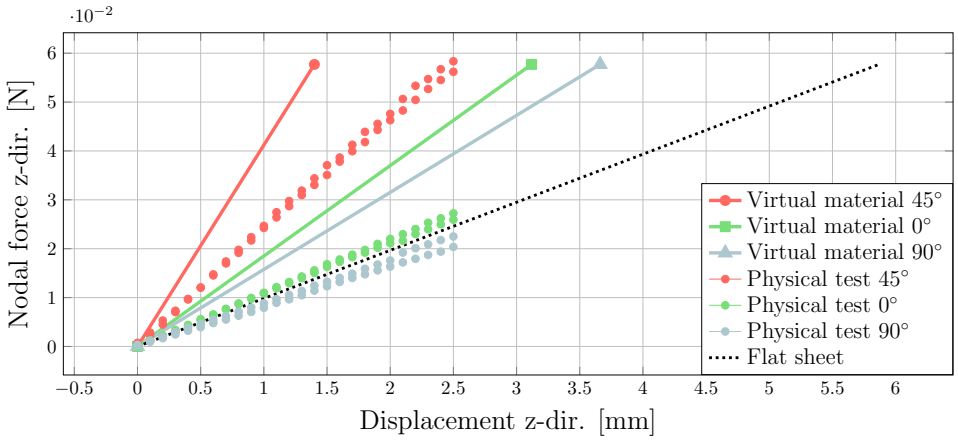

Figure 5.6: Force-displacement curves for three point bending test, geometry G4.

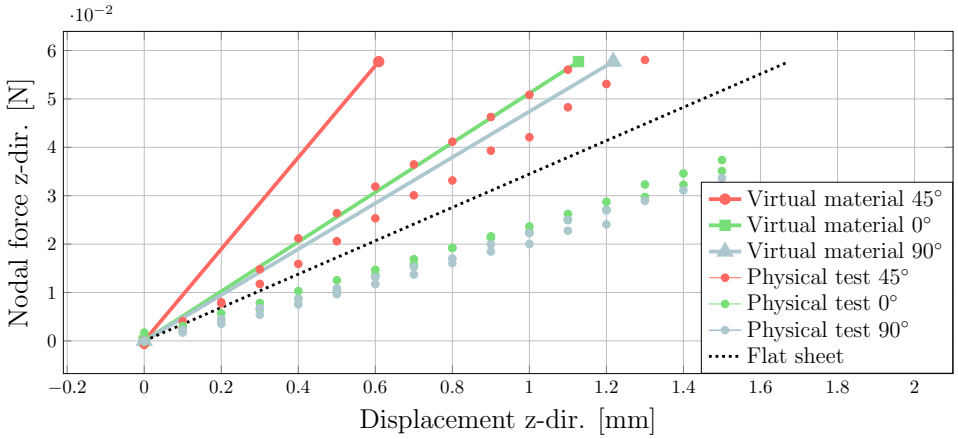

Figure 5.7: Force-displacement curves for three point bending test, geometry G6.

5.2.2 Vibration test

A modal analysis to find the heat shield's natural frequencies was done. Figure 5.8 shows two different regions of the shield; one outer region that is flat with aluminium as material (green) and one inner region where the virtual material is representing the embossed geometry (blue). The boundary conditions used were fully fixed holes according to the markings in Figure 5.8. The densities used in found in Table 3.2.

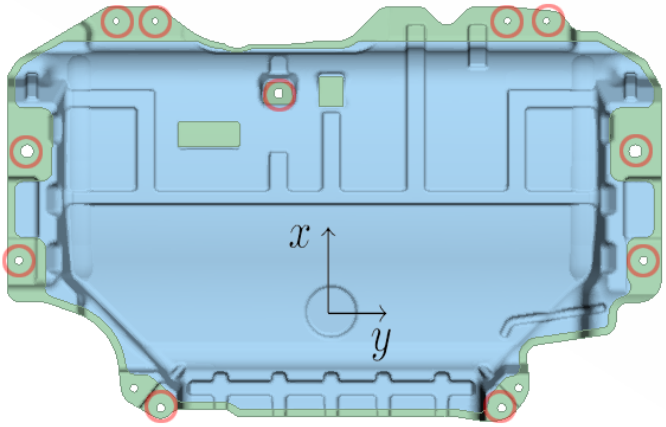

Figure 5.8: Shield model with the two regions: flat (green) and embossed (blue), and red markings where the structure is fixed.

The results in terms of the first three natural frequencies were compared to data from two types of physical tests. One test from [3] tested the shield as a single component in a vibration rig, and one from Volvo Cars where the shield was mounted on a car driving on a test track. The physical test data from both tests were available for the G4 geometry while the G6 only had data for the first natural frequency from the full car physical test. The frequency data for the two geometries are presented in Figure 5.9 and 5.10 together with the verification data. As shown, the two different types of physical data differs from each other. In this modal analysis, the test from the vibration rig is most relevant to compare to the virtual material since both of them tests only the shield component individually.

For all three modes, the virtual material model give values between the physical tests and the flat sheet. For both sheet thicknesses, the virtual material overestimates the frequencies compared to the physical tests. The material orientation does not have as large impact as it had in the three point bending test. In both G4 och G6, the difference between 45° and 0° is small, and there are no consistency in which of them that are largest.

Figures 5.11, 5.12 and 5.13 illustrates the shield geometry in the first three modes for geometry G4. The mode shapes were similar for G6, and for the different material directions.

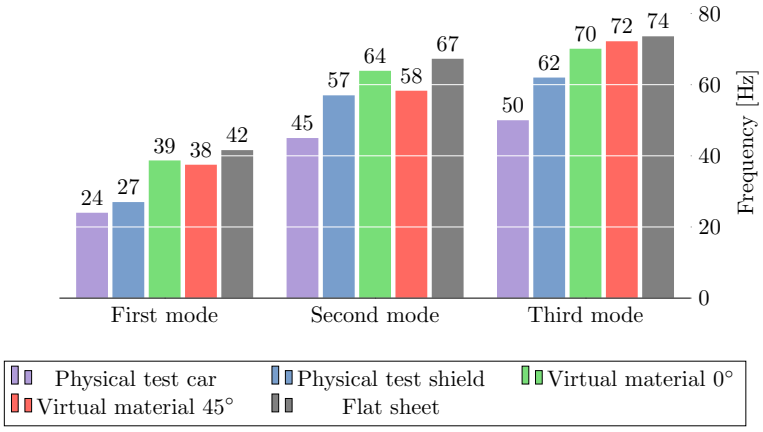

Figure 5.9: Vibration test results for geometry G4.

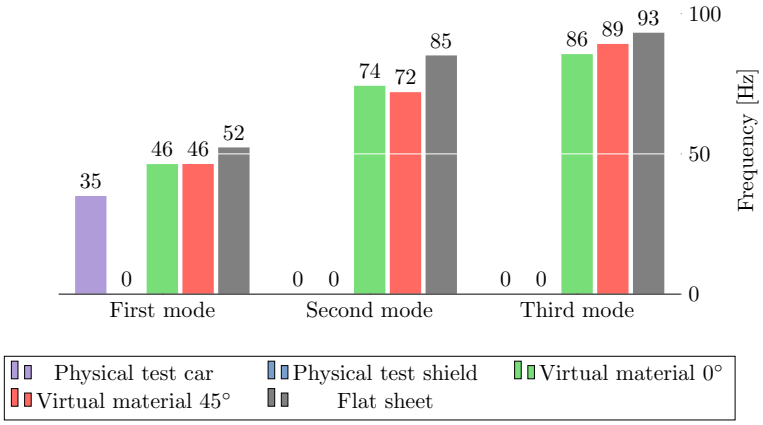

Figure 5.10: Vibration test results for geometry G6.

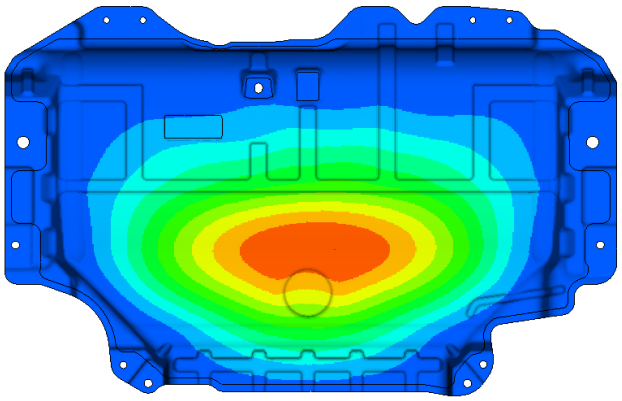

Figure 5.11: First mode, geometry G4 0°.

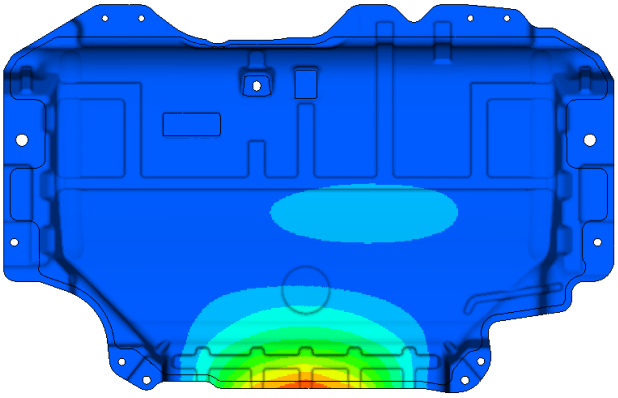

Figure 5.12: Second mode, geometry G4 0°.

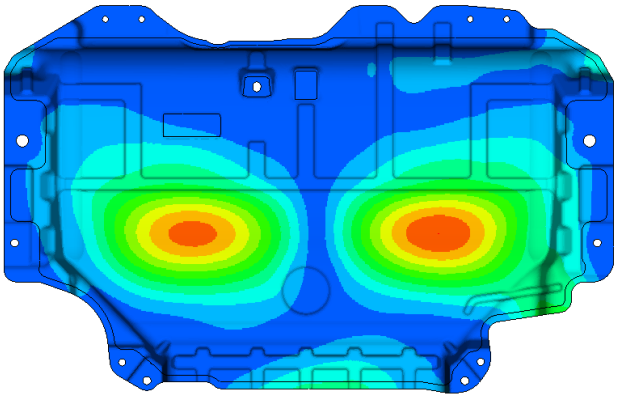

Figure 5.13: Third mode, geometry G4 0°.

6 Calibration

Since the results showed that the FE-models were significantly stiffer compared to the physical data, possible error sources were investigated in order to see if the virtual material model could be calibrated to give better resemblance.

6.1 Surface density

In an attempt to modify the virtual model to better fit the physical vibration data, the surface density was investigated to see whether this value might be wrongly estimated. The natural frequencies f depends on the density ρ_A according to the relation:

$$f \sim \frac{1}{\sqrt{\rho_A}} \tag{6.1}$$

This means that an increased density would generate lower frequencies, which is desirable for a better compliance with the physical test data. The result of this density study can be seen in Figure 6.1, and it can be seen that no specific surface density yields a good fit for all frequency modes. A surface density of $\rho_A = 0.24$ g/cm^2 gives a value close to the physical test for the first mode while $\rho_A = 0.12$ g/cm^2 fits better for the second mode and $\rho_A = 0.16$ g/cm^2 for the third mode. So it was concluded that the surface density was not the error source.

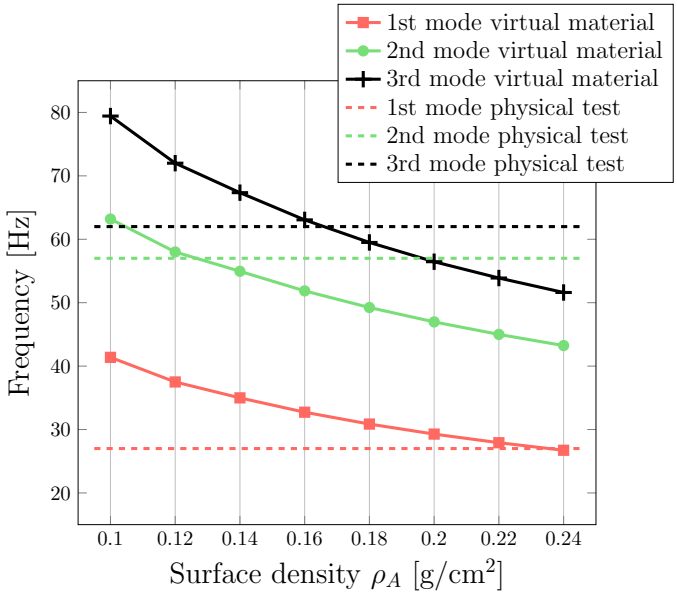

Figure 6.1: Vibration test result for surface density study of geometry G4, 0°.

6.2 Thickness

The embossed sheets were assumed to have the nominal thicknesses given by the product specifications, 0.4 mm for geometry G4 and 0.6 mm for geometry G6. These values were based on the sheet thickness before the pressing of the pattern. Based on mass data from [3], an estimated thickness was calculated from the surface area A_{emb} of the embossed sheets measured in ANSA, and the density of aluminium ρ_{al}:

$$t = \frac{m}{A_{emb}\rho_{al}} \tag{6.2}$$

The results showed that the thickness was lower compared to the assumed values. For G4 the estimated thickness was 0.34 mm and for G6 0.47 mm. To evaluate how this difference impact the results, new virtual material models based on the new thicknesses were created. These models were then tested and compared with the data from the physical tests in bending and vibration. The results from the three point bending test are presented in Figures 6.2 and 6.3, where the force-displacement curves are plotted. As shown in the graphs, the virtual material models with decreased thicknesses show much better resemblance with the physical data, compared with the original models with nominal thicknesses.

Figures 6.4 and 6.5 show the results in terms of natural frequencies from the vibration test. The surface densities used were $\rho_A = 0.103$ g/cm^2 for G4 and $\rho_A = 0.143$ g/cm^2 for G6, corresponding to the reduced thickness. The results show that the frequencies from the virtual materials for both geometries with decreased t are still too high compared to the physical test data. Although, this difference is smaller for the new models compared to the old models based on the nominal thicknesses, which implies that a decreased thickness is a better approximation.

Note that there is only one physical data point for geometry G6: the shield's first mode from the full car test. As mentioned earlier, this test is not the best one to compare the simulation output with. Better would be to compare the values with the data from the vibration test of the shield on a test rig. By the trend from the G4 data, one can assume that the physical data from the full car test predicts slightly lower frequencies compared to the data from the test rig. Considering this, the virtual model for G6 with decreased thickness t might be a good approximation of the physical shield.

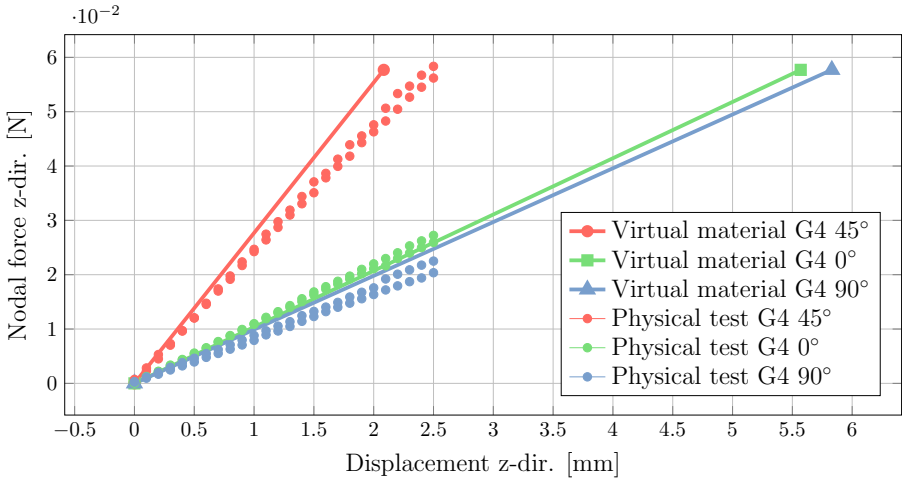

Figure 6.2: Force-displacement curves for three point bending test for geometry G4 with thickness $t = 0.34$ mm.

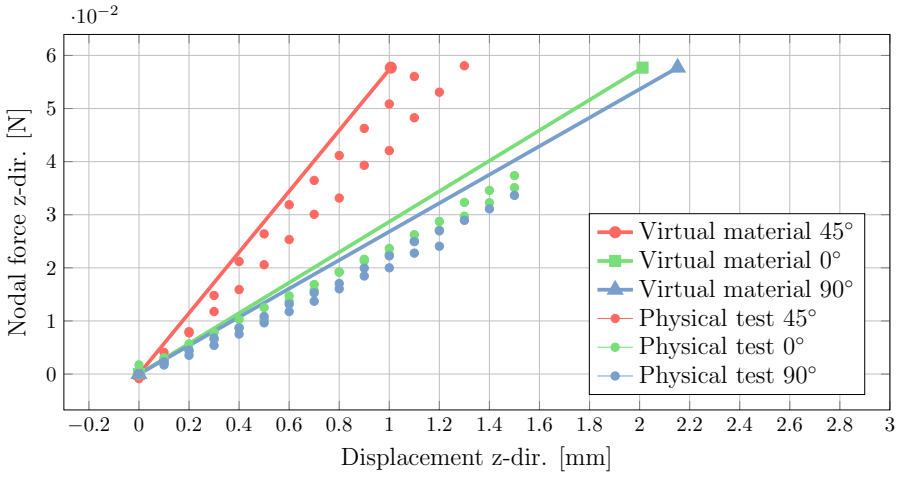

Figure 6.3: Force-displacement curves for three point bending test for geometry G6 with thickness $t = 0.47$ mm.

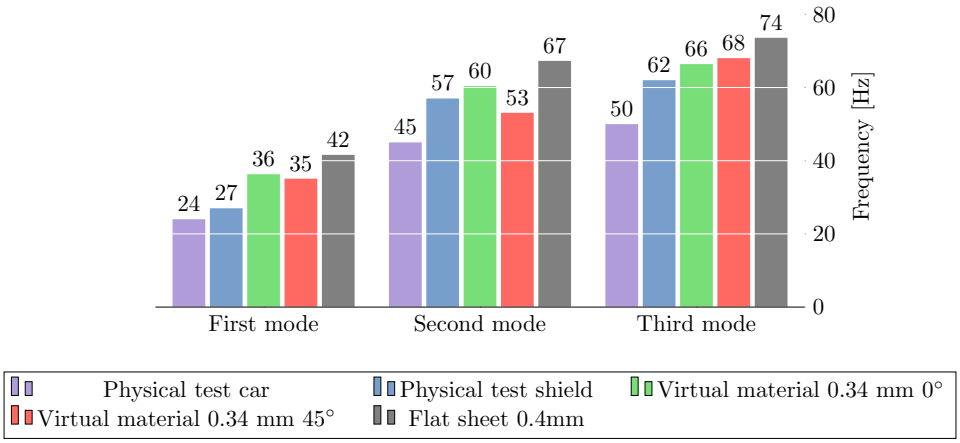

Figure 6.4: Vibration test results for geometry G4 with thickness $t = 0.34$ mm.

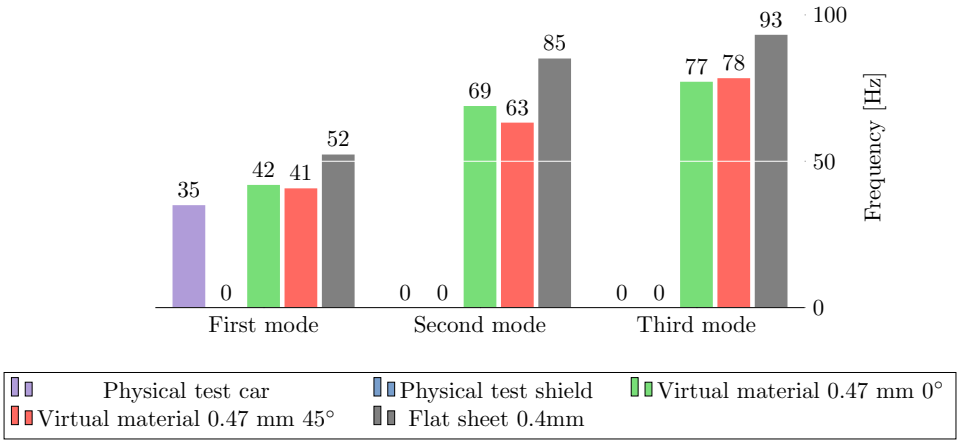

Figure 6.5: Vibration test results for geometry G6 with thickness $t = 0.47$ mm.

6.3 Flat section thickness

In the modal analysis, some regions of the heat shield are modelled with isotropic aluminium rather than the virtual material model. This is to better represent the physical heat shield which have flat regions around the outer surface and some mounting holes, see Figure 5.8. However, these flat regions were created by a pressing procedure of the already embossed structure, which means that the material properties might not correspond to the reference aluminium. To evaluate how these regions affect the results, the stiffness was changed by simulating different thicknesses. The analysis was based on geometry G4 with thickness $t = 0.34$ mm.

The result is presented in Figure 6.6, where the first three modes are plotted with the physical data as reference. A slightly lower thickness of $t = 0.3$ mm gives good resemblance with the second and third mode, while also giving slightly better resemblance for the first mode. Since there is not enough physical data available for the G6 geometry, it is however not possible to give a general recommendation.

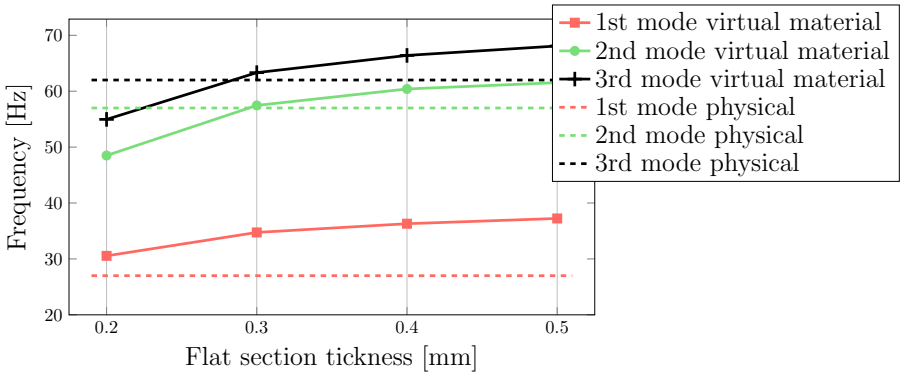

Figure 6.6: Vibration test results for geometry G4 with different flat section thicknesses.

6.4 Final virtual model

The virtual material models that best resembles with the physical data are the one with a decreased thickness based on mass data: $t = 0.34$ mm for geometry G4 and $t = 0.47$ mm for geometry G6. The stiffness matrices for these virtual material models are presented below, together with the surface density data in Table 6.1

The density and flat section thickness study did not produce any general useful models. It might be beneficial to slightly decrease the thickness of the flat section of the heat shield, but this can not be confirmed.

$$\underline{A}^{G4}_{t=0.34} = \begin{bmatrix} 1.365 & -0.223 & 0 \\ -0.228 & 1.107 & 0 \\ 0.000 & 0.000 & 0.129 \end{bmatrix} 10^4 \ \frac{\text{N}}{\text{mm}} \qquad \underline{D}^{G4}_{t=0.34} = \begin{bmatrix} 0.529 & 0.228 & 0 \\ 0.234 & 0.432 & 0 \\ 0.000 & 0.000 & 0.849 \end{bmatrix} 10^3 \ \text{Nmm}$$

$$\underline{A}^{G6}_{t=0.47} = \begin{bmatrix} 1.902 & -0.2479 & 0 \\ -0.2523 & 1.657 & 0 \\ 0.000 & 0.000 & 0.2745 \end{bmatrix} 10^4 \ \frac{\text{N}}{\text{mm}} \qquad \underline{D}^{G6}_{t=0.47} = \begin{bmatrix} 1.226 & 0.5477 & 0 \\ 0.5534 & 1.075 & 0 \\ 0.000 & 0.000 & 1.362 \end{bmatrix} 10^3 \ \text{Nmm}$$

	G4 with $t = 0.34$mm	G6 with $t = 0.47$mm
ρ_A [g/cm^2]	0.103	0.143

Table 6.1: Surface densities for the final virtual material models.

7 Parameter Study

To further understand how the embossed pattern affects the effective properties of the sheet, geometrical relations were investigated to find relationships with thickness and amplitude of the pattern.

7.1 Effect of thickness

The main stiffness components of the $\underline{A}$ and $\underline{D}$-matrices, A_{11} and D_{11}, are plotted for different thicknesses in Figure 7.1. The other geometrical parameters, amplitude and wavelength, are based on geometry G6. As expected, A_{11} increases almost linearly for increased thickness, while D_{11} increase close to cubic for increased thickness. This is due to the definition of $\underline{A}$ and $\underline{D}$, where thickness appears as t and t^3, respectively. A modal analysis was also conducted, with the result presented in Figure 7.2. The material data for all thicknesses, both in form of $\underline{A}$ and $\underline{D}$ matrices and relative elastic components, are found in Appendix G.

However, the increase for A_{11} and D_{11} is only close to, and not exact, linear or cubic. The reason is that the effect of the pattern decreases with increased thickness. For a large enough thicknesses, the embossed pattern might be negligible and the behaviour in both tension and bending would take the isotropic properties of ordinary aluminium. This is illustrated is Figure 7.3, where the normalised elastic modulus E_x in tensile and bending are plotted for different thicknesses and material directions. With increased thickness, both values indicate a convergence to the elastic modulus of aluminium, marked in black.

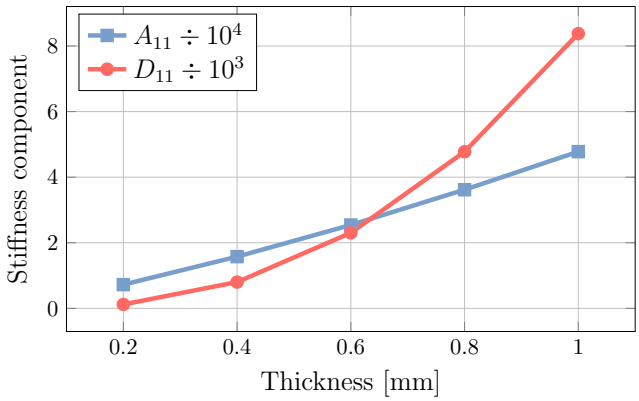

Figure 7.1: Stiffness matrix components for thickness study of geometry G6.

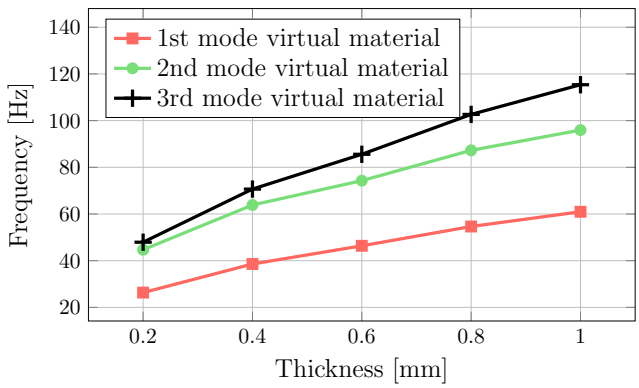

Figure 7.2: Modal analysis result for different thicknesses, based on geometry G6.

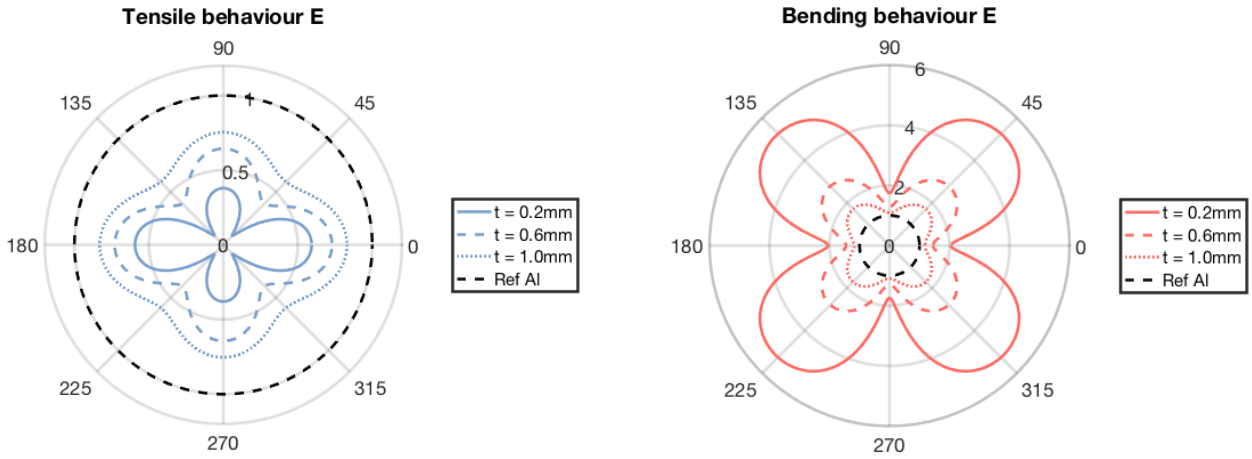

(a) Normalised tensile.

(b) Normalised bending.

Figure 7.3: The elastic modulus for different thicknesses and material directions, compared to reference Aluminium.

7.2 Effect of amplitude

To see the effect of geometrical changes of the embossed pattern, a study of the pattern amplitude was conducted. The results in Figure 7.4, where the main stiffness components A_{11} and D_{11} are plotted. With increased amplitude, the behaviour in tension becomes less stiff while the behaviour in bending becomes more stiff. In other words, the effect of the pattern increases.

The material data for all thicknesses, both in form of $\underline{A}$ and $\underline{D}$ matrices and relative elastic components, are found in Appendix G.

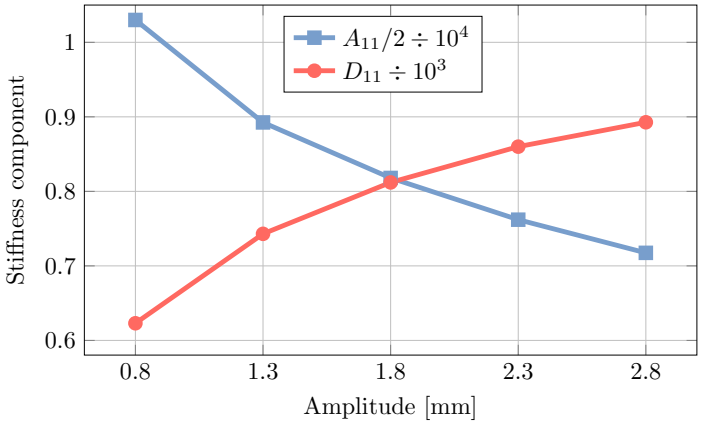

Figure 7.4: Stiffness matrix components for amplitude study of geometry G4.

A study of the natural frequencies was conducted for the amplitude as well. Since the different amplitudes changed the embossed area A_{emb}, the surface density ρ_A changed as well, see Table 7.1. The modal analysis results can be found in Figure 7.5. Despite that the bending stiffness increases with a larger amplitude, the natural frequencies decrease. This indicates that the surface density and tensile stiffness have a major contribution to the natural frequencies as well, and that embossed sheets have lower natural frequencies compared to flat sheets of the same thickness.

A [mm]	0.8	1.3	1.8	2.3	2.8
ρ_A [g/cm^2]	0.111	0.115	0.122	0.129	0.138

Table 7.1: Surface density ρ_A for different amplitudes, based on geometry G4.

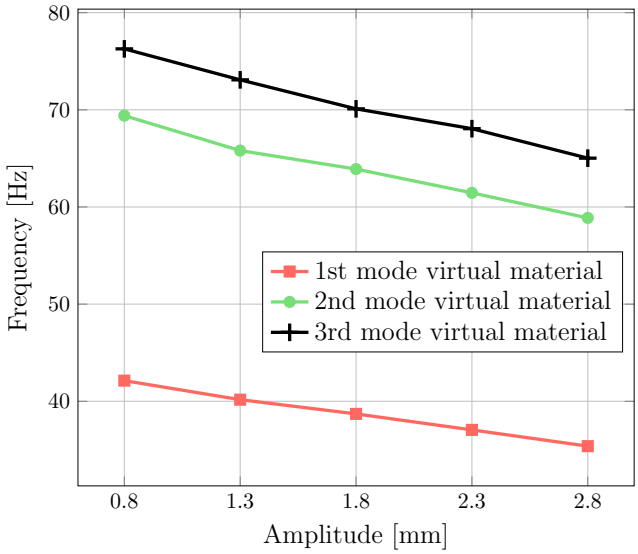

Figure 7.5: Modal analysis results for different amplitudes, based on geometry G4.

8 Discussion

This chapter discusses the results in terms of modelling of the embossed sheet, with particular focus on RVE size and boundary conditions, implementation of the virtual material model and its agreement with the different types of verification data. It also covers model calibration, parameter study and potential error sources.

Embossed sheet model

When modelling the embossed structure, both periodic (PBC) and Dirichlet (DBC) boundary conditions were investigated. In the determination of the size of the Representative Volume Element (RVE), the results showed that the PBC converged already at the smallest RVE size of 1 wavelength in each direction. The DBC needed a larger domain to reach the same values, namely an RVE with 8 wavelengths in each direction. Since the shell model of the RVE was not computationally heavy, the added complexity of the PBC compared to DBC was not justified. Thus DBC were chosen to be used for the remaining analyses in the thesis.

Implementation of virtual material

The inhomogeneous embossed structure had different tensile and bending behaviours that were described by the thickness-dependent stiffness matrices $\underline{A}$, $\underline{B}$ and $\underline{D}$. This made every virtual material model valid only for the thickness it was derived from. This means that the virtual material model could not be implemented in terms of the normal material properties E, ν and G, like the trivial input in FE-simulations. Instead, the model was implemented by defining its stiffness matrices in tension and bending, $\underline{A}$ and $\underline{D}$, directly into Abaqus. Other implementation methods that were discussed, but not tested, were material sets in MSC NASTRAN and a laminate with tensile and bending properties in different layers.

Virtual material vs FE-verification

In tension, the derived virtual material model corresponded well to a fully resolved embossed FE-model. The difference was less than 1% for geometry G4 and less than 2% for geometry G6. Compared to a flat aluminium sheet with the same thickness, the embossed sheet was less stiff. This is due to the fact that the embossed pattern was stretched-out when exposed to the tensile load, a process that requires less force compared to when elongating a flat aluminium structure.

In bending, however, the embossed sheet was found to be significantly stiffer in comparison with an FE-model of a flat aluminium sheet. The derived virtual material did not comply as well with the fully resolved embossed FE-model as in tension. The FE-model were 19% stiffer for G4 and 14% stiffer for G6. One possible error source is the simplification made to the implementation of the DBC. Though, the stiffness of the virtual material was much closer to the embossed FE-model compared to the FE-model of a flat aluminium sheet.

Virtual material vs Physical test data

When comparing the derived material model to physical data, it became clear that the virtual material was significantly stiffer. It was demonstrated both in the 3-point bending test and in the vibration test, where the natural frequencies were higher than expected. Since the virtual material, on the other hand, showed good resemblance with the fully resolved FE-model, it was suspected there might exist error sources in the modelling of the embossed sheets. A likely one is that certain characteristics of the actual structure failed to be captured when creating the FE-model of the embossed structure. This will be discussed in the following section.

Calibration and final virtual material model

It was assumed that the sheet thicknesses were the nominal values specified for each sheet, namely 0.4 and 0.6 mm. But based on physical mass data, calculations showed that the averaged thicknesses were indeed thinner than suggested: 0.34 and 0.47 mm. The new virtual material derived from these thicknesses showed a very good resemblance to the physical bending tests, and also better results in the vibration test, why this became the final virtual material model. This material does not perfectly match the physical vibration test data, but it is a much better approximation in comparison with a flat aluminium sheet with equivalent thicknesses.

Error sources

A possible error source to why the virtual material model does not exactly match the physical data, especially in the vibration test, could be that the actual thickness might vary along the embossed pattern. This effect could change the stiffness in certain areas of the shield, and was not taken into account.

Further, in the modal analysis of the heat shield, the shield was simulated as completely fixed in the mountings. This could be an error source since in reality, these are probably not that stiff.

Others error sources could be effects from the manufacturing method. Even though the thickness was adjusted, the stamping process might also have effected the sheet by leaving residual stresses in the structure, something that was not taken into account. Also, in addition to the stamping of the pattern, the final shield is also formed to its heat shield shape. This process might also affect the properties, which would explain why the three point bending test, using small specimens, showed better resemblance compared to the vibration test of the complete heat shield.

There could also be sources of error in the physical testing methods. For example, the two different physical data from the vibration test differed quite significantly from each other.

Parameter study

When the thickness increases, both tensile and bending stiffness increase as well. For a sufficiently thick plate, the material response converges to that of isotropic aluminium. One reason for this is that the amplitude stayed the same during the study, and hence the ratio A/t became smaller with an increased thickness.

When increasing the pattern amplitude, the tensile stiffness decreased while the bending stiffness and the surface density increased. Theoretically, this effect should result in higher frequencies for the increased bending stiffness and lower frequencies due to the decreased tensile stiffness and increased surface density. The results showed that the frequencies were in fact lower than before, which implies that the tensile stiffness and surface density combined had larger impact compared to the bending stiffness. This is also confirmed in the amplitude study and by the fact that a flat sheet predicts higher natural frequencies compared to an embossed sheet.

9 Conclusions

In this thesis, homogenisation was used to develop a virtual material model that describes the averaged macroscopic behaviour of an embossed aluminium sheet and enables it to be analysed as a flat structure. The embossed pattern was modelled mathematically and analysed using the FE method to identify the mechanical properties according to the homogenisation procedure virtual material testing. The method generated thickness dependent virtual material models that describes the embossed sheets' tensile and bending behaviours in terms of the corresponding stiffness matrices. The virtual material models were tested to investigate their agreement with fully resolved embossed FE-models and physical test data. The project's main conclusions are listed below.

- The embossed structure can advantageously be modelled mathematically using expressions that describes the pattern as harmonic curves in different directions.
- Compared to a flat aluminium sheet, the embossed pattern adds stiffness to the structure in bending but provides a degraded performance under tensile loads. This is due to the pattern-stretch that dominates the response in pure tension. Together with an increased surface density, this results in natural frequencies that are lower for an embossed heat shield compared to a flat sheet.
- When comparing the virtual material on a flat structure with an embossed FE-model with aluminium as material, the results showed that the homogenisation method worked well to predict the tensile behaviour but slightly less well in bending.
- On the tests that examined the agreement with the physical test data, the virtual material model showed results that were stiffer than the measured values. However, when using a modified thickness based on mass calculations instead of the nominal thickness, the model gives a good agreement with the physical bending data, while the vibration data still gives higher natural frequencies.
- Likely error sources might be the neglected effects from the manufacturing process of the embossed sheets. Examples are residual stresses in the structure and varying thickness in the pattern. It could also be error sources in the physical test data.

9.1 Future work

In order to create a virtual material model with better agreement to the physical test data, a more extensive study about the manufacturing effects is suggested. Also, to get better correspondence with the fully resolved embossed FE-model, the homogenisation method, in particular bending, should be reviewed. In order to gain better results in general, it would be advantageous with more physical test data of the embossed structure. As a suggestion, tests where different thicknesses are tested in tensile, bending, shear and vibration loading scenarios.

References

[1] R. M. Harrison et al. *Environmental Impacts of Road Vehicles: Past, Present and Future*. Cambridge: Royal Society of Chemistry, The LaVergne: Ingram Publisher Services [Distributor], 2017.

[2] Laurent Laszczyk. *Homogenization and topological optimization of architectured panels*. Universite de grenoble, 2006.

[3] Cai Öhrvall. *Evaluation of vibration testing method for aluminium heat shield*. Chalmers University of Technology, 2018.

[4] Beta CAE. *ANSA Pre-processor, Version 18.1.1*. `https://www.beta-cae.com/ansa.htm`. Accessed: 2018-09-30.

[5] Dassault Systèmes. *Abaqus/Standard, Version 2016*. `https://www.3ds.com/products-services/simulia/products/abaqus/`. Accessed: 2018-09-30.

[6] Beta CAE. *META Post-processor, Version 18.0.0*. `https://www.beta-cae.com/meta.htm`. Accessed: 2018-09-30.

[7] MathWorks. *Matlab Version R2016a*. `https://se.mathworks.com/products/matlab.html`. Accessed: 2018-09-30.

[8] Tomasz Kubiak. *Static and Dynamic Buckling of Thin-Walled Plate Structures*. Springer International Publishing Switzerland, 2013.

[9] Dassault Systèmes. *Abaqus 2016 Documentation*. `http://130.149.89.49:2080/v2016/index.html`. Accessed: 2018-10-22.

[10] Fredrik Larsson and Kenneth Runesson. *Introduction to finite element analysis of plates*. Chalmers university of Technology, 2014.

[11] Magnus Ekh. *Mechanics of solids and fluids - Elasticity and structural mechanics*. Chalmers University of Technology, 2016.

[12] Piaras Kelly. *Lecture notes: Solid Mechanics Part II: Engineering Solid Mechanics – small strain*. The University of Auckland, 2015.

[13] Piaras Kelly. *Lecture notes: An Introduction to Solid Mechanics*. The University of Auckland, 2015.

[14] Bhagwan D. Agarwal and Lawrence J. Broutman and K. Chandrashekhara. *Analysis and performance of fiber composites*. John Wiley and Sons Inc, 2006.

[15] Ragnar Larsson and Fredrik Larsson. *Lecture notes in Material Mechanics: Homogenized material properties*. 2012.

[16] Weidong Wu and Joseph Owino and Ahmed Al-Ostaz and Liguang Cai. *Applying Periodic Boundary Conditions in Finite Element Analysis*. Department of Civil, Chemical Engineering, University of Tennessee at Chattanooga, and Department of Civil Engineering, The University of Mississippi, 2014.

[17] Sadik L. Omairey and Peter D. Dunning and Srinivas Sriramula. *Development of an ABAQUS plugin tool for periodic RVE homogenisation*. 2018.

[18] J. Blaauwendraad. *Plates and FEM - Surprises and Pitfalls*. Springer, Dordrecht, 2010.

[19] Richard Routledge, Encyclopedia Britannica, Inc. *Least squares method*. https://academic-eb-com.proxy.lib.chalmers.se/levels/collegiate/article/least-squares-method/384411. Accessed: 2018-10-27.

[20] MathWorks. *fminsearch*. https://www.mathworks.com/help/matlab/ref/fminsearch.html. Accessed: 2018-10-27.

[21] Magnus Ekh. *Mechanics of solids and fluids - Introduction to continuum mechanics*. Chalmers University of Technology, 2016.

[22] Tomislav Lesičar. *Multiscale Modeling of Heterogeneous Materials Using Second-Order Homogenization*. Universite of Zagreb, 2015.

[23] Srihari Kurukuri. *Homogenization of Damaged Concrete Meso-structures using Representative Volume Elements*. Institute of Structural Mechanics, Bauhaus–University Weimar, 2005.

Appendices

A Quick guide: virtual material implementation

Since the virtual material model have different material behaviours in tension and bending, it cannot be implemented in FE-software as ordinary material properties, E, ν and G. Instead, the implementation method used is to directly specify the stiffness matrices $\underline{A}$, $\underline{B}$ and $\underline{D}$ using the command *Shell general section* in Abaqus. No other material definition is required. Since the thickness is not defined, it is the surface area that is specified, see Section 3.2. The $\underline{B}$-matrix can be omitted (defined as zero) since it was shown that its effect on the result is negligible. An example of an input file is given below. This method is also described in Section 4.3. A complete Abaqus input file with the material definitions needed to model a heat shield is found in Appendix D.

```
*SHELL GENERAL SECTION, ELSET=elements, DENSITY=surface_density ,ORIENTATION=orientation
A11,A12,A22,A13,A23,A33,B11,B21
B31,D11,B12,B22,B32,D12,D22,B13
B23,B33,D13,D23,D33
```

The virtual material models that showed best resemblance with the physical test were the ones where decreased thicknesses were used instead nominal thicknesses. For geometry G4 this was $t = 0.34$ mm and for geometry G6 $t = 0.47$ mm. The surface densities for these values are found in Table A.1. This final virtual material model is also described in Section 6.4.

When simulating the heat shield, the outer flat section (see Figure 5.8) have been modelled as isotropic aluminium with the same thickness as the virtual model.

$$\underline{A}^{G4}_{t=0.34} = \begin{bmatrix} 1.365 & -0.223 & 0 \\ -0.228 & 1.107 & 0 \\ 0.000 & 0.000 & 0.129 \end{bmatrix} 10^4 \ \frac{\text{N}}{\text{mm}} \qquad \underline{D}^{G4}_{t=0.34} = \begin{bmatrix} 0.529 & 0.228 & 0 \\ 0.234 & 0.432 & 0 \\ 0.000 & 0.000 & 0.849 \end{bmatrix} 10^3 \ \text{Nmm}$$

$$\underline{A}^{G6}_{t=0.47} = \begin{bmatrix} 1.902 & -0.2479 & 0 \\ -0.2523 & 1.657 & 0 \\ 0.000 & 0.000 & 0.2745 \end{bmatrix} 10^4 \ \frac{\text{N}}{\text{mm}} \qquad \underline{D}^{G6}_{t=0.47} = \begin{bmatrix} 1.226 & 0.5477 & 0 \\ 0.5534 & 1.075 & 0 \\ 0.000 & 0.000 & 1.362 \end{bmatrix} 10^3 \ \text{Nmm}$$

	G4 $t = 0.34$	G6 $t = 0.47$
ρ_A [g/cm^2]	0.103	0.143

Table A.1: Surface density ρ_A for the final virtual material models.

B Quick guide: create new virtual materials

This guide describes briefly how to create new virtual material models, which can be helpful when evaluating new embossed sheet geometries.

Embossed sheet model

Study the new embossed geometry and identify parameters: amplitude, A, wavelength in both direction, a, b, and thickness, t. The thickness is not necessarily the nominal thickness specified by manufacturers, but rather below that value. The "real" thickness can be calculated based on for example mass data, as in Equation 6.2.

Use Matlab script *create embossed surfaces* to create a surface file in stl-format. This will create a surface based on the function in Equation 3.1. The code is found in Appendix C.

The surface density ρ_A will increase due to the embossed pattern and is calculated based on the change in surface area. This is explained in Section 3.2.

Virtual material testing

The created geometry will represent a new RVE of the embossed sheet. This thesis concluded that an the RVE domain size of 8x8 wavelengths were sufficient. Import the RVE into for example ANSA and re-mesh it into quad elements with a base size of 0.1mm. Define sets for all edges and corners, as well as the middle node.

Conduct the six different virtual material tests. Simulation output needs to be reaction forces $\underline{N}$ and reaction moments $\underline{M}$. The boundary conditions, in terms of displacements $\underline{u}^0$ and rotations $\underline{\alpha}$, are described in Section 2.3. Dirichlet boundary conditions are recommended. The loading conditions used are described in Section 4.1.2. Note that for the tension tests, the displacement value should be halved if the displacement is applied on two opposite boundaries while the middle node is fixed.

Identify virtual stiffness matrices

From the inputs, $\underline{u}^0$ and $\underline{\alpha}$, calculate the strains $\underline{\epsilon}^0$ and curvatures $\underline{\kappa}$ using Equation 2.9 and 2.10. Together with the output $\underline{N}$ and $\underline{M}$, the stiffness matrices can now be identified using Equation B.1.

$$\begin{bmatrix} \underline{N} \\ \underline{M} \end{bmatrix} = \begin{bmatrix} \underline{A} & \underline{B} \\ \underline{B} & \underline{D} \end{bmatrix} \begin{bmatrix} \underline{\epsilon}^0 \\ \underline{\kappa} \end{bmatrix} \tag{B.1}$$

For the first test with ϵ^0_{xx} =value, identify the first column of $\underline{A}$ and $\underline{B}$ using Equation B.2.

$$\begin{aligned} \underline{N}_{xx} &= A_{11}\epsilon^0_{xx} \\ \underline{N}_{yy} &= A_{12}\epsilon^0_{xx} \\ \underline{N}_{xy} &= A_{16}\epsilon^0_{xx} \\ \underline{M}_{xx} &= B_{11}\epsilon^0_{xx} \\ \underline{M}_{yy} &= B_{12}\epsilon^0_{xx} \\ \underline{M}_{av} &= B_{16}\epsilon^0_{xx} \end{aligned} \tag{B.2}$$

The reaction forces and moments are calculated as the sum over the boundaries according to Equation B.3. The boundary-notation used refers to Figure 3.8 with n and m defined as the reaction quantities node-wise.

$$
\begin{aligned}
\underline{N}_{xx} &= \frac{1}{L_{East}} \sum_{East} N_{xx} \\
\underline{N}_{yy} &= \frac{1}{L_{North}} \sum_{North} N_{yy} \\
\underline{N}_{xy} &= \frac{1}{L_{East}} \sum_{East} N_{yy} + \frac{1}{L_{North}} \sum_{North} n_{xx} \\
\underline{M}_{xx} &= \frac{1}{L_{East}} \sum_{East} M_{xx} \\
\underline{M}_{yy} &= \frac{1}{L_{North}} \sum_{North} M_{yy} \\
\underline{M}_{xy} &= \frac{1}{L_{East}} \sum_{East} M_{yy} + \frac{1}{L_{North}} \sum_{North} m_{xx}
\end{aligned}
\tag{B.3}
$$

For bending, the south and west boundaries might be used instead depending on the direction of the applied rotation.

Follow this procedure for all six virtual tests to produce all the stiffness matrices $\underline{A}$, $\underline{B}$ and $\underline{D}$.

Implement the virtual material model

The material is implemented using the stiffness matrices as described in Appendix A.

C Matlab code: create embossed surfaces

```
%-------------------------------------------------------------------------
%
% Create surface models of embossed sheet based on geometry input
%
% Requires function "surf2stl"
%
% Written by Filip Ljungstr?m in the autumn of 2018 as a part of the master
% thesis "homogenization of embossed aluminium sheets using virtual
% material testing" togehter with Sofia Alexandersson. The thesis is
% conducted at FS Dynamics for Volvo Cars
%
%-------------------------------------------------------------------------
close all; clear all; clc

% ---------------------------------
%         Input
% ---------------------------------
plotType = 2; %1 = mesh, 2 = surface (does not change the output-file)

% Geometry
A = 1.87;       % Amplitude
X_per = 8.086;  % Period in x-dir (a)
Y_per = 7.41;   % Period in y-dir (b)

% Domain properties
n_per_X = 8;            % Number of periods in domain x-direction
n_per_Y = 8;            % Number of periods in domain y-direction
res_x = 90*n_per_X;     % Number of cells in x-direction
res_y = 90*n_per_Y;     % Number of cells in y-direction

% ---------------------------------
%         End of input
% ---------------------------------

%%%%%%%%%% Calculations %%%%%%%%%%
L_dom_x = X_per*n_per_X; % Length of domain in X
L_dom_y= Y_per*n_per_Y;

a = (X_per/(2*pi))^(-1); % Convert "length to period"
b = (Y_per/(2*pi))^(-1);

%Creates grid
[X,Y] = meshgrid(linspace(0,L_dom_x,res_x),linspace(0,L_dom_y,res_y));

%Creates mathematical function
zx = sin(a*(X-X_per/2));
zy = sin(b*Y);
Z = (A/2)*(zx.*zy);

% Puts the origo in center
X = X - (X_per*n_per_X)/2;
Y = Y - (Y_per*n_per_Y)/2;

%%%%%%%%% Plot the result %%%%%%%%%
figure()
if plotType == 1
    mesh(X,Y,Z)
    mymap = [0 0 0];
    colormap(mymap)
    hold on
    plot(0,0,'*')
elseif plotType == 2
    surf(X,Y,Z)
    colormap bone
end
shading interp
axis([-L_dom_x/2 L_dom_x/2 -L_dom_y/2 L_dom_y/2 -2.5*A 2.5*A])
```

```
68 xlabel('x')
69 ylabel('y')
70 zlabel('z')
71 title('Waffel surface')
72
73 %%%%%%%%%% Export stl model %%%%%%%%%
74
75 surf2stl('Size_study/filename.stl',X,Y,Z)
```

D Abaqus input file: material definition heat shield

```
**
** Abaqus input file for modelling heat shield with virtual material model
** ... in form of stiffness matrices A,B,D. Two element sets must be defined,
** ... one for inner embossed section and one for outer flat section
**
** Input file created by Sofia Alexandersson and Filip Ljungstrom as part of the
** ... master thesis "Homogenisation of embossed aluminium sheets using virtual
** ... material testing" in the autumn of 2018
**
**
** ----------------------------------------------
** Input parameters
** ----------------------------------------------
**
*Parameter
flat_section_thickness = 0.
surface_density = 0.
**
A11 = 0.
A12 = 0.
A22 = 0.
A13 = 0.
A23 = 0.
A33 = 0.
**
** (B = 0)
B11 = 0.
B12 = 0.
B22 = 0.
B13 = 0.
B23 = 0.
B33 = 0.
**
**
D11 = 0.
D12 = 0.
D22 = 0.
D13 = 0.
D23 = 0.
D33 = 0.
**
**
** ----------------------------------------------
** Flat Section
** ----------------------------------------------
**
**
*SHELL SECTION, ELSET=Flat_Section, MATERIAL=Al
                      <flat_section_thickness>,
**
*MATERIAL, NAME=Al
*DENSITY
                   2.70E-9,
*ELASTIC, TYPE=ISOTROPIC
                    69000.,                        0.33
**
**
**
** ----------------------------------------------
** Embossed Section
**----------------------------------------------
**
*SHELL GENERAL SECTION,ELSET=Embossed_Section,DENSITY=<surface_density>
<A11>,<A12>,<A22>,<A13>,<A23>,<A33>,<B11>,<B12>
<B13>,<D11>,<B12>,<B22>,<B23>,<D12>,<D22>,<B13>
<B23>,<B33>,<D13>,<D23>,<D33>
**
```

E Additional boundary conditions

Here the MPC equations for periodic boundaries in shear are presented. Equation E.1 refers to the edge conditions and Equation E.2 for the corner conditions.

$$\begin{aligned} u_1^{West} - u_1^{East} - &= 0 \\ u_1^{South} - u_1^{North} - u_{1,dummy} &= 0 \\ u_2^{West} - u_2^{East} - u_{2,dummy} &= 0 \\ u_2^{South} - u_2^{North} &= 0 \\ \alpha_4^{West} - \alpha_4^{East} &= 0 \\ \alpha_4^{South} - \alpha_4^{North} &= 0 \\ \alpha_5^{West} - \alpha_5^{East} &= 0 \\ \alpha_5^{South} - \alpha_5^{North} &= 0 \end{aligned} \tag{E.1}$$

$$\begin{aligned} u_1^{nw} - u_1^{se} - u_{1,dummy} &= 0 \\ u_1^{sw} - u_1^{ne} - u_{1,dummy} &= 0 \\ u_2^{nw} - u_2^{se} - u_{2,dummy} &= 0 \\ u_2^{sw} - u_2^{ne} - u_{2,dummy} &= 0 \end{aligned} \tag{E.2}$$

Table E.1 presents the DBC for twisting.

	→	→	→	↺	↺	↺
	1	2	3	4	5	6
West	0	0	free	$-\alpha_4$	0	free
East	0	0	free	α_4	0	free
North	0	0	free	0	$-\alpha_5$	free
South	0	0	free	0	α_5	free
nw	0	0	free	$-\alpha_4$	$-\alpha_5$	free
sw	0	0	free	$-\alpha_4$	α_5	free
ne	0	0	free	α_4	$-\alpha_5$	free
se	0	0	free	α_4	α_5	free

Table E.1: Symmetric Dirichlet boundary conditions for $\bar{\kappa}_{xy}$.

F Level of Anisotropy G4

Below is the plots for elastic modulus E and shear modulus G for different material directions presented for geometry G4. They are normalised and compared to the value of isotropic aluminium.

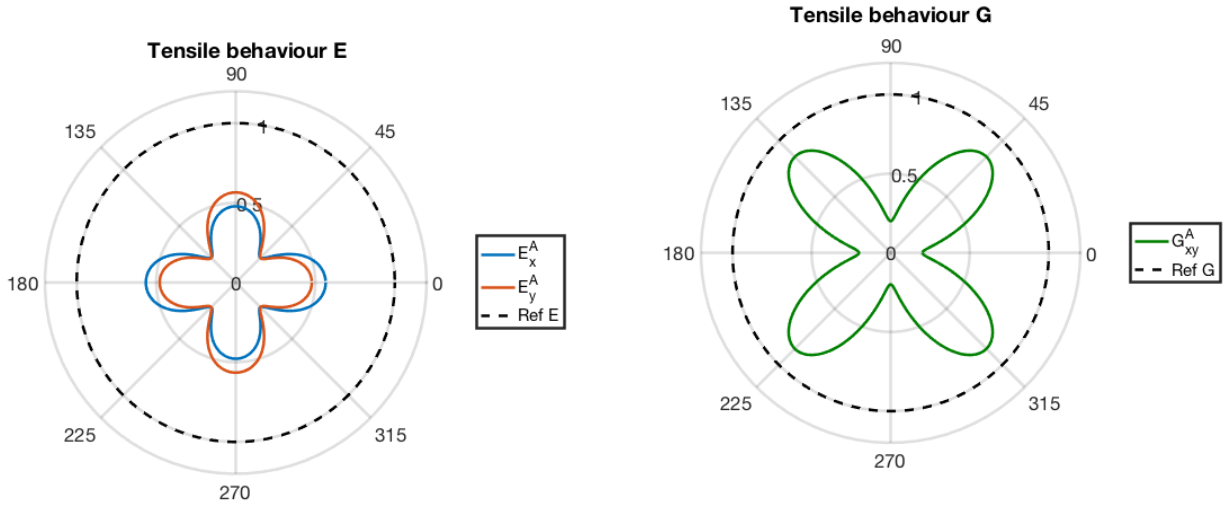

Figure F.1: Normalised in-plane modulus and shear modulus tensile behaviour for G4.

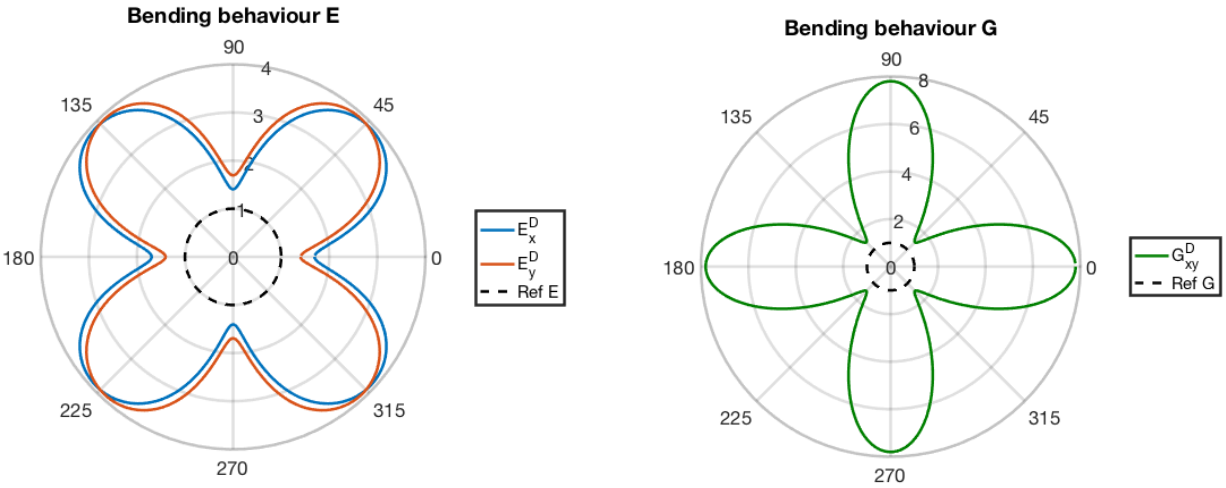

Figure F.2: Normalised in-plane modulus and shear modulus bending behaviour for G4

G Virtual material models in parameter study

This section presents the material data for the different virtual materials from the parametric study.

G.1 Thickness

Data from the thickness study.

$$\underline{A}^{G6}_{t=0.2} = \begin{bmatrix} 0.724 & -0.160 & 0 \\ -0.162 & 0.612 & 0 \\ 0.000 & 0.000 & 0.028 \end{bmatrix} 10^4 \ \frac{\text{N}}{\text{mm}} \quad \underline{D}^{G6}_{t=0.2} = \begin{bmatrix} 0.120 & 0.051 & 0 \\ 0.053 & 0.103 & 0 \\ 0.000 & 0.000 & 0.480 \end{bmatrix} 10^3 \text{ Nmm}$$

$$\underline{A}^{G6}_{t=0.4} = \begin{bmatrix} 1.577 & -0.242 & 0 \\ -0.246 & 1.364 & 0 \\ 0.000 & 0.000 & 0.183 \end{bmatrix} 10^4 \ \frac{\text{N}}{\text{mm}} \quad \underline{D}^{G6}_{t=0.4} = \begin{bmatrix} 0.802 & 0.376 & 0 \\ 0.364 & 0.697 & 0 \\ -0.001 & 0.000 & 1.11 \end{bmatrix} 10^3 \text{ Nmm}$$

$$\underline{A}^{G6}_{t=0.8} = \begin{bmatrix} 3.618 & -0.110 & 0 \\ -0.117 & 3.241 & 0 \\ 0.000 & 0.000 & 0.896 \end{bmatrix} 10^4 \ \frac{\text{N}}{\text{mm}} \quad \underline{D}^{G6}_{t=0.8} = \begin{bmatrix} 4.777 & 2.035 & 0 \\ 2.045 & 4.34 & 0 \\ -0.001 & 0.000 & 2.95 \end{bmatrix} 10^3 \text{ Nmm}$$

$$\underline{A}^{G6}_{t=1.0} = \begin{bmatrix} 4.779 & 0.087 & 0 \\ 0.080 & 4.335 & 0 \\ 0.000 & 0.000 & 1.36 \end{bmatrix} 10^4 \ \frac{\text{N}}{\text{mm}} \quad \underline{D}^{G6}_{t=1.0} = \begin{bmatrix} 8.378 & 3.496 & 0 \\ 3.507 & 7.743 & 0 \\ 0.000 & 0.000 & 4.306 \end{bmatrix} 10^3 \text{ Nmm}$$

	E_x [GPa]	E_y [GPa]	ν_{xy} [-]	ν_{yx} [-]	G_{xy} [GPa]
t = 0.2 [mm]	34.11	28.82	-0.261	-0.223	1.39
t = 0.4 [mm]	38.33	33.15	-0.118	-0.156	4.58
t = 0.6 [mm]	41.98	37.04	-0.100	-0.090	8.13
t = 0.8 [mm]	45.18	40.47	-0.034	-0.032	11.20
t = 1.0 [mm]	47.77	43.33	0.020	0.018	13.60

Table G.1: Relative material properties for geometry G6 for thickness study, tensile behaviour.

	E_x [GPa]	E_y [GPa]	ν_{xy} [-]	ν_{yx} [-]	G_{xy} [GPa]
t = 0.2 [mm]	141.10	120.20	0.498	0.437	720.30
t = 0.4 [mm]	113.50	98.66	0.540	0.450	207.20
t = 0.6 [mm]	99.96	89.12	0.490	0.440	106.00
t = 0.8 [mm]	89.48	81.32	0.469	0.428	69.18
t = 1.0 [mm]	81.53	75.36	0.451	0.419	51.67

Table G.2: Relative material properties for geometry G6 for thickness study, bending behaviour.

G.2 Amplitude

Data from the pattern amplitude study.

$$\underline{A}^{G4}_{A=0.8} = \begin{bmatrix} 2.059 & -0.027 & 0 \\ -0.031 & 1.806 & 0 \\ 0.000 & 0.000 & 0.531 \end{bmatrix} 10^4 \ \frac{\text{N}}{\text{mm}} \qquad \underline{D}^{G4}_{A=0.8} = \begin{bmatrix} 0.624 & 0.263 & 0 \\ 0.267 & 0.549 & 0 \\ 0.000 & 0.000 & 0.619 \end{bmatrix} 10^3 \ \text{Nmm}$$

$$\underline{A}^{G4}_{A=1.3} = \begin{bmatrix} 1.785 & -0.202 & 0 \\ -0.207 & 1.498 & 0 \\ 0.000 & 0.000 & 0.304 \end{bmatrix} 10^4 \ \frac{\text{N}}{\text{mm}} \qquad \underline{D}^{G4}_{A=1.3} = \begin{bmatrix} 0.743 & 0.324 & 0 \\ 0.331 & 0.627 & 0 \\ -0.001 & 0.000 & 0.705 \end{bmatrix} 10^3 \ \text{Nmm}$$

$$\underline{A}^{G4}_{A=2.3} = \begin{bmatrix} 1.524 & -0.227 & 0 \\ -0.232 & 1.240 & 0 \\ 0.000 & 0.000 & 0.138 \end{bmatrix} 10^4 \ \frac{\text{N}}{\text{mm}} \qquad \underline{D}^{G4}_{A=2.3} = \begin{bmatrix} 0.860 & 0.368 & 0 \\ 0.372 & 0.705 & 0 \\ -0.001 & 0.000 & 1.334 \end{bmatrix} 10^3 \ \text{Nmm}$$

$$\underline{A}^{G4}_{A=2.8} = \begin{bmatrix} 1.435 & -0.204 & 0 \\ -0.209 & 1.162 & 0 \\ 0.000 & 0.000 & 0.107 \end{bmatrix} 10^4 \ \frac{\text{N}}{\text{mm}} \qquad \underline{D}^{G4}_{A=2.8} = \begin{bmatrix} 0.893 & 0.373 & 0 \\ 0.379 & 0.727 & 0 \\ 0.000 & 0.000 & 1.541 \end{bmatrix} 10^3 \ \text{Nmm}$$

	E_x [GPa]	E_y [GPa]	ν_{xy} [-]	ν_{yx} [-]	G_{xy} [GPa]
A = 0.8 [mm]	51.46	45.15	-0.015	-0.015	13.28
A = 1.3 [mm]	43.94	36.85	-0.135	-0.116	7.60
A = 1.8 [mm]	39.84	32.78	-0.175	-0.147	4.90
A = 2.3 [mm]	37.05	30.13	-0.183	-0.152	3.46
A = 2.8 [mm]	34.96	28.30	-0.175	-0.145	2.67

Table G.3: Relative material properties for amplitude study of geometry G4, tensile behaviour.

	E_x [GPa]	E_y [GPa]	ν_{xy} [-]	ν_{yx} [-]	G_{xy} [GPa]
A = 0.8 [mm]	93.03	81.90	0.478	0.428	116.10
A = 1.3 [mm]	107.30	90.51	0.517	0.445	132.80
A = 1.8 [mm]	116.80	96.84	0.525	0.443	195.40
A = 2.3 [mm]	124.70	102.20	0.522	0.434	250.30
A = 2.8 [mm]	131.02	106.70	0.513	0.424	288.90

Table G.4: Relative material properties for amplitude study of geometry G4, bending behaviour.